



NRL/MR/5310--10-9312

RF Photonic, In-Situ, Real-Time Phased Array Antenna Calibration System

W. MARK DORSEY

MARK G. PARENT

S. ANDREW LONG

Radar Analysis Branch

Radar Division

CHRISTOPHER S. McDERMITT

FRANK BUCHOLTZ

Photonics Technology Branch

Optical Sciences Division

November 22, 2010

REPORT DOCUMENTATION PAGE

Form Approved
OMB No. 0704-0188

Public reporting burden for this collection of information is estimated to average 1 hour per response, including the time for reviewing instructions, searching existing data sources, gathering and maintaining the data needed, and completing and reviewing this collection of information. Send comments regarding this burden estimate or any other aspect of this collection of information, including suggestions for reducing this burden to Department of Defense, Washington Headquarters Services, Directorate for Information Operations and Reports (0704-0188), 1215 Jefferson Davis Highway, Suite 1204, Arlington, VA 22202-4302. Respondents should be aware that notwithstanding any other provision of law, no person shall be subject to any penalty for failing to comply with a collection of information if it does not display a currently valid OMB control number. **PLEASE DO NOT RETURN YOUR FORM TO THE ABOVE ADDRESS.**

| | | | | | | | | | |
|---------------------------------------------------------------------------------------------------------------------------------------------------------------------------------------------------------------------------------------------------------------------------------------------------------------------------------------------------------------------------------------------------------------------------------------------------------------------------------------------------------------------------------------------------------------------------------------------------------------------------------------------------------------------------------------------------------------------------------------------------------------------------------------------------------------------------------------------------------------------------------------------------------------------------------------------------------------------------------------------------------------------------------------------------------------------------------------------------------------------------------------------------------------------------------------------------------------------|--|--------------------|--------------------------------------------|---------------------|--|-----------------------------------------------------------------------------|----------------------------|--------------------------------------------------------------------|--|
| 1. REPORT DATE (DD-MM-YYYY) 22-11-2010 | | | 2. REPORT TYPE Memorandum Report | | | 3. DATES COVERED (From - To) September 2004 - September 2008 | | | |
| 4. TITLE AND SUBTITLE RF Photonic, In-Situ, Real-Time Phased Array Antenna Calibration System | | | | | | 5a. CONTRACT NUMBER | | | |
| | | | | | | 5b. GRANT NUMBER | | | |
| | | | | | | 5c. PROGRAM ELEMENT NUMBER | | | |
| 6. AUTHOR(S) W. Mark Dorsey, Mark G. Parent, S. Andrew Long, Christopher S. McDermitt, and Frank Bucholtz | | | | | | 5d. PROJECT NUMBER 53-6242-0-85 | | | |
| | | | | | | 5e. TASK NUMBER | | | |
| | | | | | | 5f. WORK UNIT NUMBER 6242 | | | |
| 7. PERFORMING ORGANIZATION NAME(S) AND ADDRESS(ES) Naval Research Laboratory 4555 Overlook Avenue, SW Washington, DC 20375-5320 | | | | | | 8. PERFORMING ORGANIZATION REPORT NUMBER NRL/MR/5310--10-9312 | | | |
| 9. SPONSORING / MONITORING AGENCY NAME(S) AND ADDRESS(ES) Naval Research Laboratory, Code 5300 4555 Overlook Avenue, SW Washington, DC 20375-5320 | | | | | | 10. SPONSOR / MONITOR'S ACRONYM(S) NRL | | | |
| | | | | | | 11. SPONSOR / MONITOR'S REPORT NUMBER(S) | | | |
| | | | | | | | | | |
| 12. DISTRIBUTION / AVAILABILITY STATEMENT Approved for public release; distribution is unlimited. | | | | | | | | | |
| 13. SUPPLEMENTARY NOTES | | | | | | | | | |
| 14. ABSTRACT The next generation of Navy ships will incorporate the latest in advanced electronics, weapon systems and antenna aperture structures to support the future needs of the Navy. Phased array antennas are typically comprised of 1000's of elements and are able to electronically steer multiple beams throughout a prescribed sector to provide both search and targeting information. This very timely information is usually integrated with other systems onboard a platform for use in situation awareness. Currently, without proper and frequent calibration, signal errors from environmental fluctuations and component aging result in diminished performance of the array. Due to the complex and dynamic nature of these active aperture systems, real-time system calibration will be required to maintain the ability to operate at the high level of performance necessary to carry out a platform mission. A collaborative effort between the Radar Division and Optical Sciences Division of the U.S. Naval Research Laboratory has successfully demonstrated a system with performance suitable for in-situ, real-time calibration of shipboard phased array antennas. | | | | | | | | | |
| 15. SUBJECT TERMS Phased array Frequency selective service Calibration Radome | | | | | | | | | |
| 16. SECURITY CLASSIFICATION OF: | | | | | | 17. LIMITATION OF ABSTRACT | 18. NUMBER OF PAGES | 19a. NAME OF RESPONSIBLE PERSON | |
| a. REPORT | | b. ABSTRACT | | c. THIS PAGE | | UU | 58 | W. Mark Dorsey | |
| Unclassified | | Unclassified | | Unclassified | | | | 19b. TELEPHONE NUMBER (include area code) (202) 404-5639 | |

Table of Contents

| | |
|-------------------------------------------------------------------------------------------------------|-----|
| Table of Figures | iv |
| Executive Summary | E-1 |
| 1 INTRODUCTION | 1 |
| 2 PHOTONICS SUBSYSTEM..... | 4 |
| 2.1 Characterization of Zero Bias Photodiodes..... | 6 |
| 2.1.1 Zero Bias Photodiodes – Setup..... | 8 |
| 2.1.2 Zero Bias Photodiodes – Measurements..... | 9 |
| 2.2 Hardware and Components | 18 |
| 2.3 Time Trimming | 20 |
| 3 RF SUBSYSTEMS..... | 22 |
| 3.1 Design and Performance of Electrically Short Dipole Antenna (ESDA) | 22 |
| 3.1.1 Induced Voltage Simulations..... | 23 |
| 3.1.2 Integration of Photodiode into ESDA..... | 25 |
| 3.2 Design and Performance of a Bandpass Frequency Selective Surface with Integrated Photodiodes..... | 26 |
| 3.3 Design and Performance of a Broadband Dipole Array | 32 |
| 4 SYSTEM PERFORMANCE AND STABILITY..... | 35 |
| 4.1 Photonic System Stability | 35 |
| 4.2 Stability of Calibration Signal: Photodiode to Antenna Element Coupling..... | 40 |
| 4.3 RF Transparency of Frequency Selective Surface with Integrated Photonic Calibration System..... | 45 |
| 5 CONCLUSIONS..... | 48 |
| REFERENCES | 49 |

Table of Figures

| | |
|---------------------------------------------------------------------------------------------------------------------------------------------------------------------------------------------------------------------------------------------------------------------------------------------------------------------------------------------------------------------------------------------------------------------|----|
| Figure 1-1: Naval Research Laboratory Radar Division Near-Field Scanner | 3 |
| Figure 2-1: Architecture for an in-situ phased-array calibration system employing an array of zero-biased photodiodes (PD) each driving a small patch antenna (PA) all embedded in a frequency-selective surface (FSS) and mounted adjacent to the RF receive antenna array. Each photodiode receives RF-modulated light by means of a single-mode optical fiber through an optical distribution network (ODN)..... | 4 |
| Figure 2-2: Block diagram of photonic subsystem for phased array antenna calibration system .. | 5 |
| Figure 2-3: Top view photograph of the optical distribution network (ODN) | 5 |
| Figure 2-4: Front view photograph of the optical distribution network (ODN)..... | 6 |
| Figure 2-5: Microscope image with dimensions of the external packaging of zero bias photodiode..... | 7 |
| Figure 2-6: Photonic link used for photodiode measurements. The RF input method varied depending on the test at hand. The different test systems were designed for each measurement objective..... | 8 |
| Figure 2-7: Photodiode measurement circuit diagrams. a) photovoltaic measurement circuit and b)RF measurement circuit with bias tee..... | 9 |
| Figure 2-8: Open-circuit photodiode voltage, short-circuit photocurrent, and the 50 Ω load photocurrent as a function of input optical power. | 10 |
| Figure 2-9: Voltage-current curves of photodiodes at zero-bias. The circles represent experimental data. The solid lines represent theory from (1) with $R_s = 10 \Omega$ | 10 |
| Figure 2-10: PD RF output power at 2 GHz as a function of reverse bias voltage for various optical power levels. | 13 |
| Figure 2-11: RF output power from zero-bias photodiode as a function of input optical power with 2 GHz RF input to the MZM at -18.5 , -8.5 , and 1.5 dBm. | 13 |
| Figure 2-12: The measured RF output power as a function of optical input power and the RF output power calculated from the slope of the $I_{50\Omega}$ curve in Fig. 4. Inset shows the difference in the RF output power predicted from $I_{50\Omega}$ and the measured power in Fig. 2-11. | 15 |
| Figure 2-13: Frequency response of the photodiode at 0 and 5 V reverse bias from 50 MHz to 8 GHz. An optical input power of 2.5 mW and RF input power of 5 dBm is used..... | 15 |
| Figure 2-14: Photodiode harmonic distortion phase locked loop measurement setup. | 16 |

Figure 2-15: Fundamental and harmonic response of photodiodes with an incident optical input at 1 GHz absent any harmonic content by means of a heterodyned laser setup. The heterodyne system is designed so the DC photocurrent remains constant, in this case at 1 mA. 17

Figure 2-16: Output intercept point of the second and third harmonic (OIP2 and OIP3 respectively) as a function of applied reverse bias. 1 GHz input tone with 1 mA DC photocurrent. The circles represent the OIP2 and the squares represent the OIP3. 17

Figure 2-18: Attenuation vs. applied electric voltage for variable optical attenuators 19

Figure 2-19: Variable optical attenuator stability over time 19

Figure 2-20: Bar graph displaying the individual output optical power range for 16 VOA's 20

Figure 3-1: Architecture for phased-array calibrator employing an array of zero-biased photodiodes (PD) each driving an electrically short dipole (ESDA). Each PD receives RF-modulated light from a single-mode optical fiber through an optical distribution network (ODN). 22

Figure 3-2: Illustration of the shape for an electrically short dipole antenna (ESDA) with location of integrated photodiode circled 23

Figure 3-3: Simulation model used to study the voltage induced on a diode placed across the gap of an electrically short dipole antenna (ESDA) 24

Figure 3-4: Simulated Electric Field Distribution in S-band Waveguide Containing an electrically short dipole antenna with a diode placed across the gap 24

Figure 3-5: Simulated voltage across a diode placed in the gap of an electrically short dipole antenna (ESDA) resulting from a 1W TE₁₀ waveguide mode 25

Figure 3-6: (a) Shape of the electrically short dipole antenna (ESDA) used for integrating photodiodes into a frequency selective surface, (b) Photograph of external electrical connection pads of the 25

Figure 3-7: Detailed drawing showing the integration of the photodiode with the dipole probe. 26

Figure 3-8: Top view (a) and dielectric profile (b) of a frequency selective surface (FSS) with 2.5-2.5GHz passband 27

Figure 3-9: Dimensioned drawing of the frequency selective surface (FSS) unit cell with integrated dipole probe and photodiode (units = cm) 28

Figure 3-10: Electric field definitions for the TE and TM mode used in simulations of the FSS unit cell 29

| | |
|---------------------------------------------------------------------------------------------------------------------------------------------------------------------------------|----|
| Figure 3-11: Simulated transmission coefficient of FSS unit cell for multiple scan angles..... | 30 |
| Figure 3-12: Illustration of the printed circuit board layers for 10 x 10 FSS panels containing (a) 0, (b) 10, and (c) 100 electrically short dipole antenna (ESDA) probes..... | 31 |
| Figure 3-13: Measured transmission coefficient through FSS panels with various numbers of optical calibration probes compared to a baseline unit cell simulation | 32 |
| Figure 3-14: Illustration of Broadband Dipole Element fed with Double Marchand Balun | 33 |
| Figure 3-15: Simulated Active Element Return Loss | 33 |
| Figure 3-16: Constructed Double Marchand Balun Dipole Elements | 34 |
| Figure 3-17: Measured radiation patterns for multiple rows of the broadband dipole array fed with a dual Marchand balun..... | 34 |
| Figure 4-1: Amplitude and Phase Response of Stability Measurement: Day 1..... | 36 |
| Figure 4-2: Amplitude and Phase Response of Stability Measurement: Day 2..... | 36 |
| Figure 4-3: Amplitude and Phase Response of Stability Measurement: Day 3..... | 37 |
| Figure 4-4: Amplitude and Phase Response of Stability Measurement: Day 4..... | 37 |
| Figure 4-5: Amplitude and Phase Response of Stability Measurement: Day 5..... | 38 |
| Figure 4-6: Standard Deviation for Initial Amplitude and Phase Response | 38 |
| Figure 4-7: Standard Deviation for Amplitude and Phase Response: Day 2-5 | 39 |
| Figure 4-8: Amplitude and Phase Stability | 40 |
| Figure 4-9: Optical Calibration FSS Panel Integrated in Front of Broadband Dipole Array | 41 |
| Figure 4-10: Optical calibration probe-to-antenna element coupling measurement setup | 41 |
| Figure 4-11: Illustration of the s-parameters measured for the optical probe-to-antenna element coupling measurements..... | 42 |
| Figure 4-12: Average s_{12} results for optical probe coupling measurements..... | 43 |
| Figure 4-13: Normalized s_{12} results for optical probe coupling measurements..... | 43 |
| Figure 4-14: Root Mean Squared Error at 3GHz..... | 44 |
| Figure 4-15: Average Root Mean Squared Error vs. Frequency | 45 |

Figure 4-16: Photographs of the fabricated frequency selective surface with integrated photonic calibration system for phased array antennas 46

Figure 4-17: Measured radiation pattern of a 16-element dipole array with and without the presence of the FSS with integrated optical calibration system components 47

Figure 4-18: Measured active element VSWR for an array element with and without the presence of a frequency selective surface (FSS) with integrated photonic calibration network 47

Executive Summary

The next generation of Navy ships will incorporate the latest in advanced electronics, weapon systems and antenna aperture structures to support the future needs of the Navy. Phased array antennas are typically comprised of 1000's of elements and are able to electronically steer multiple beams throughout a prescribed sector to provide both search and targeting information. This very timely information is usually integrated with other systems onboard a platform for use in situation awareness. Currently, without proper and frequent calibration, signal errors from environmental fluctuations and component aging result in diminished performance of the array. Due to the complex and dynamic nature of these active aperture systems, real-time system calibration will be required to maintain the ability to operate at the high level of performance necessary to carry out a platform mission. A collaborative effort between the Radar Division and Optical Sciences Division of the U.S. Naval Research Laboratory has successfully demonstrated a system with performance suitable for in-situ, real-time calibration of shipboard phased array antennas that:

- **Easily integrates into current systems:** incorporates a multi-layer radome structure containing an array of calibration probes mounted directly in front of the phased array radar. The probes are fed via photonic signals – allowing the control unit to be remotely located on the platform.
- **Is RF transparent to avoid interference:** the integration of the radome containing the photonic calibration system and frequency selective surface is essentially RF-transparent and would, therefore, be suitable for in-situ calibration without degrading the performance of the phased array radar.
- **Offers stable and highly reliable calibration signals:** all 16 elements of the calibration array have a standard deviation of less than 0.3 dB for magnitude and less than 2.5° for phase. The average standard deviation across the channels as a function of frequency was consistent over the entire operation frequency bandwidth.
- **Provides a foundation to confidently initiate a high-impact 6.3 program:** the results of this research exceeded expectations in meeting performance requirements and presents the opportunity for the Navy to move forward with a high-impact 6.3 program to expedite this advanced technology to the field.

1 INTRODUCTION

The next generation of Navy ships, such as the LCS, DDX or CVN, will incorporate the latest in advanced electronics, weapon systems and antenna aperture structures to support the future needs of the Navy. These systems are designed to minimize the number of ship personnel needed to operate these systems while providing advanced capabilities currently unavailable to the Navy war fighters. The major shift in ship design can be observed from the replacement of distributed antenna system with imbedded apertures located in the ship's superstructure. These antenna apertures are being integrated into the ship's superstructure to improve the ship's overall radar cross section (RCS) while removing the need for mechanically stabilized antennas. With these advancements, the next generation of ships will provide the Navy with an advanced attack force and fleet presence for the next several decades to come. In order for these systems to be maintained and operated at high performance levels, new advanced built-in tests and calibration techniques must be incorporated into the overall system concept. This report describes an optical calibration technique that can be integrated into a multi-layer radome structure, which can be used for various calibration and simulation procedures.

All antennas have errors associated with them. In the case of phased array systems, these errors are caused by the misalignment of both the amplitude and phase values in each element signal path. The combination of these errors can cause a reduction in gain, degradation in sidelobe levels and monopulse accuracy as well as a host of other electrical performance issues. Phased array antennas are typically comprised of 1000's of elements and are able to electronically steer multiple beams throughout a prescribed sector to provide both search and targeting information. This very timely information is usually integrated with other systems onboard a platform for use in situation awareness. Due to the complex and dynamic nature of these active aperture systems, real-time system calibration will be required to maintain the ability to operate at the high level of performance necessary to carry out a platform mission.

With the development of array antennas, many techniques have been proposed to perform initial calibration on the antenna system. Phased array antennas are utilized in applications including radar, communications, and electronic warfare (EW). The performance of these phased arrays can be degraded by environmental effects including temperature, mechanical stresses, and vibration as well as long-term aging of system components [1].

A common calibration technique for large phased array apertures utilizes a calibration signal transmitted from an external source located away from the aperture of the phased array [2-4]. However, the presence of the external sources in the techniques described in [2-4] has the disadvantage of requiring a source that is not co-located with the array. The external source is often difficult to realize on vehicle platforms and requires additional real estate that is seldom available.

One of the most useful tools available for array calibration is the near-field scanner [5]. Near-field scanning techniques provide a convenient method to measure both amplitude and phase distribution across the array face. Figure 1-1 shows a typical planar near-field scanner. Unfortunately, once an array system is placed into operation, the array is typically not recalibrated unless a major fault or repair is required. Several programs [6, 7] have developed transportable near field scanning systems that enabled a method to recheck the calibration after a system has been placed in service. Though these systems are very useful for specific applications, their use in ship based systems is limited due to real-time calibration requirements. As array antenna systems incorporate advanced functions and capabilities they will require real-time alignment procedures to maintain their peak performance.

Shipboard phased arrays currently lack a means for in-situ, real-time calibration. All antennas have errors associated with them. In the case of phased array systems, these errors are caused by the misalignment of both the amplitude and phase values in each element signal path. Without proper and frequent calibration, signal errors from environmental fluctuations and component aging result in diminished performance with respect to gain, degradation in sidelobe levels, monopulse accuracy, and other standard metrics [8]. Phased array antennas are typically comprised of 1000's of elements and are able to electronically steer multiple beams throughout a prescribed sector to provide both search and targeting information. This very timely information is usually integrated with other systems onboard a platform for use in situation awareness. Due to the complex and dynamic nature of these active aperture systems, real-time system calibration will be required to maintain the ability to operate at the high level of performance necessary to carry out a platform mission. Current technology such as near-field scanners and transportable calibration systems present significant practical limitations for real-time, in-situ calibration. Critical aspects for integrating an on-board phased-array antenna calibration system (PAACS) are 1) RF transparency within the operational frequency band and 2) sufficient temporal stability in amplitude and phase of the calibration signals. However, it should be noted that fluctuations in the calibration signals are tolerable, provided they are minimal, and more importantly, that the deviations are common across all channels. The figure of merit used to verify the stability and repeatability of our calibration system is the standard deviation of the amplitude and phase fluctuations of each channel.



Figure 1-1: Naval Research Laboratory Radar Division Near-Field Scanner

The calibration technique described in this report uses an optical method consisting of photodiodes integrated within a frequency selective surface (FSS) that is placed in front of the phased array aperture. This has the advantage of providing a compact calibration system that can be co-located with the phased array, thus minimizing the size requirements for the overall system. The RF-modulated optical signal is detected by a zero-biased photodiode, and the RF signal excites electrically small dipole antennas (ESDAs) that are integrated in the FSS panel located in front of the phased array elements. The signal transmitted by the ESDA to the element in the array serves as the calibration signal.

This report details the design and implementation of the calibration technique. The photonic subsystems used to generate the calibration signal are detailed and characterized. This is followed by a discussion of the RF subsystems – including a band pass frequency selective surface with integrated electrically short dipole antennas and a broadband dipole array. After describing the operation of the individual subsystems, the performance of the calibration system is presented through investigations into system stability and RF transparency.

2 PHOTONICS SUBSYSTEM

The photonic phased array antenna calibration system (PAACS) illustrated in Figure 2-1 consists of photonics and RF subsystems. The components of the photonic system are outlined in the block diagram shown in Figure 2-2. A distributed feedback (DFB) laser operating at 1550 nm is externally modulated with a Mach-Zehnder modulator (MZM). The modulated light is optically amplified with an erbium doped fiber amplifier (EDFA) and distributed through a 16-fiber ribbon cable to an array of photodiodes. Within the optical distribution network (ODN), the amplitude and phase of each channel is controlled in the optical domain via in-line, voltage-controlled variable optical attenuators and by phase trimming the physical length of fiber. After photodetection, the RF calibration signals are applied directly to an array of electrically small dipole antennas (ESDA). The photo detectors are operated without bias voltage [9] eliminating the need for electrical wiring and avoiding potential interference effects due to mutual-coupling. Hence, each optical element transmits a calibration signal to the adjacent element of the receive array. Top and front views of the ODN are shown in Figures 2-3 and 2-4 respectively. The performance and design of the ODN are described in the remainder of this section.

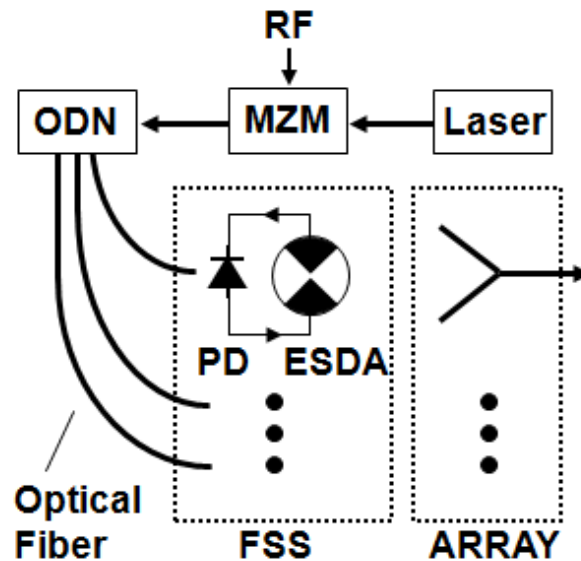


Figure 2-1: Architecture for an in-situ phased-array calibration system employing an array of zero-biased photodiodes (PD) each driving a small patch antenna (PA) all embedded in a frequency-selective surface (FSS) and mounted adjacent to the RF receive antenna array. Each photodiode receives RF-modulated light by means of a single-mode optical fiber through an optical distribution network (ODN).

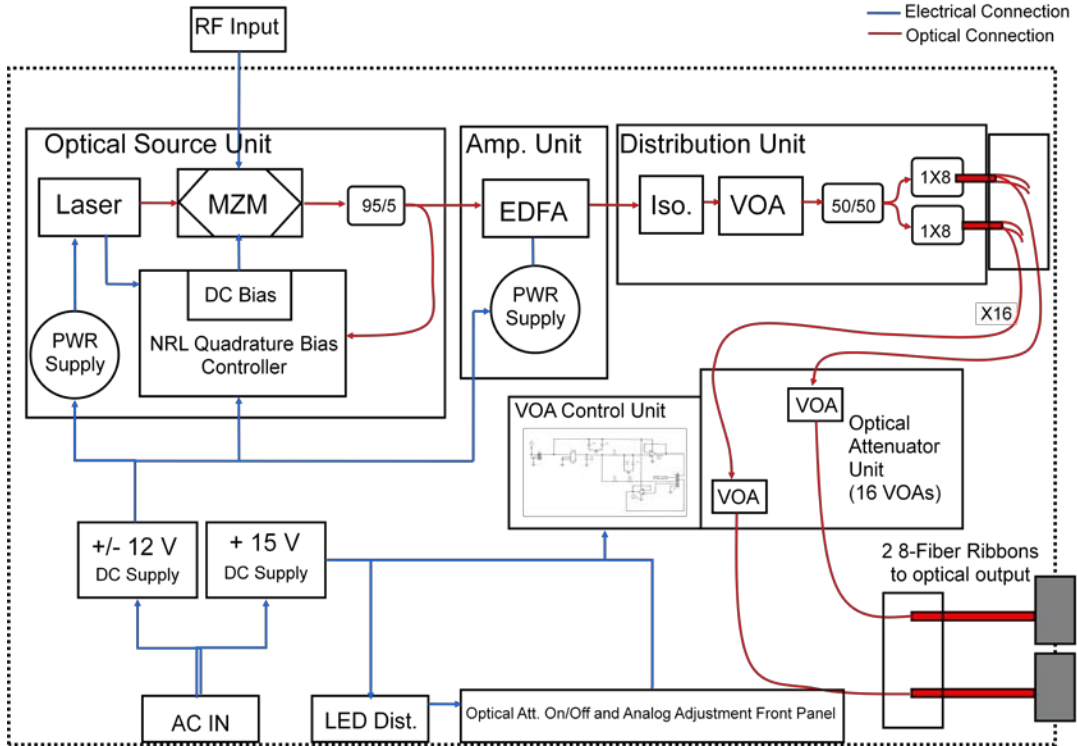


Figure 2-2: Block diagram of photonic subsystem for phased array antenna calibration system

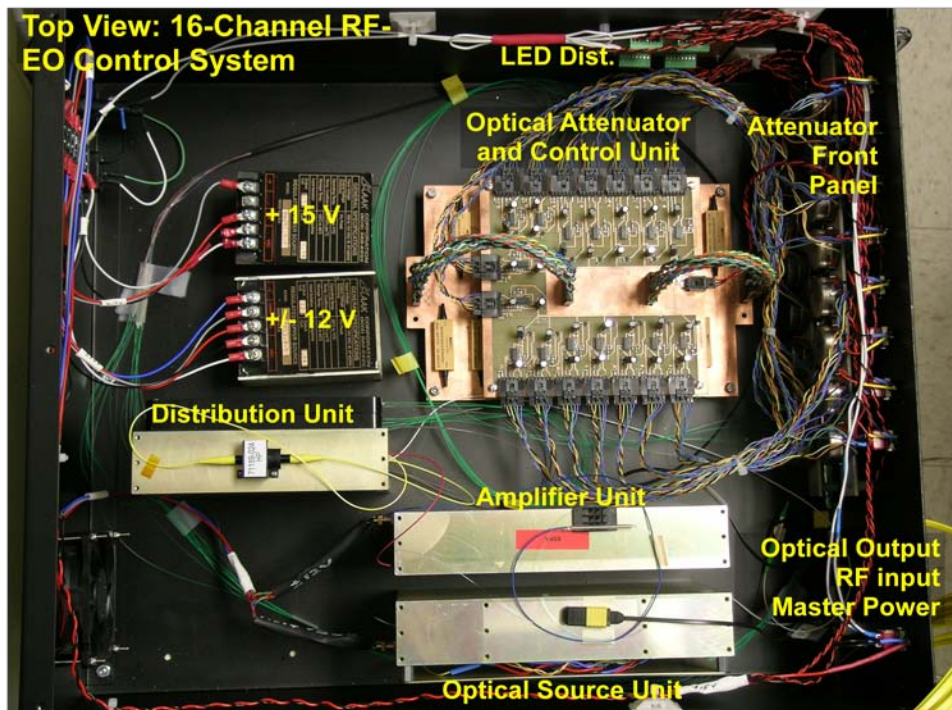


Figure 2-3: Top view photograph of the optical distribution network (ODN)

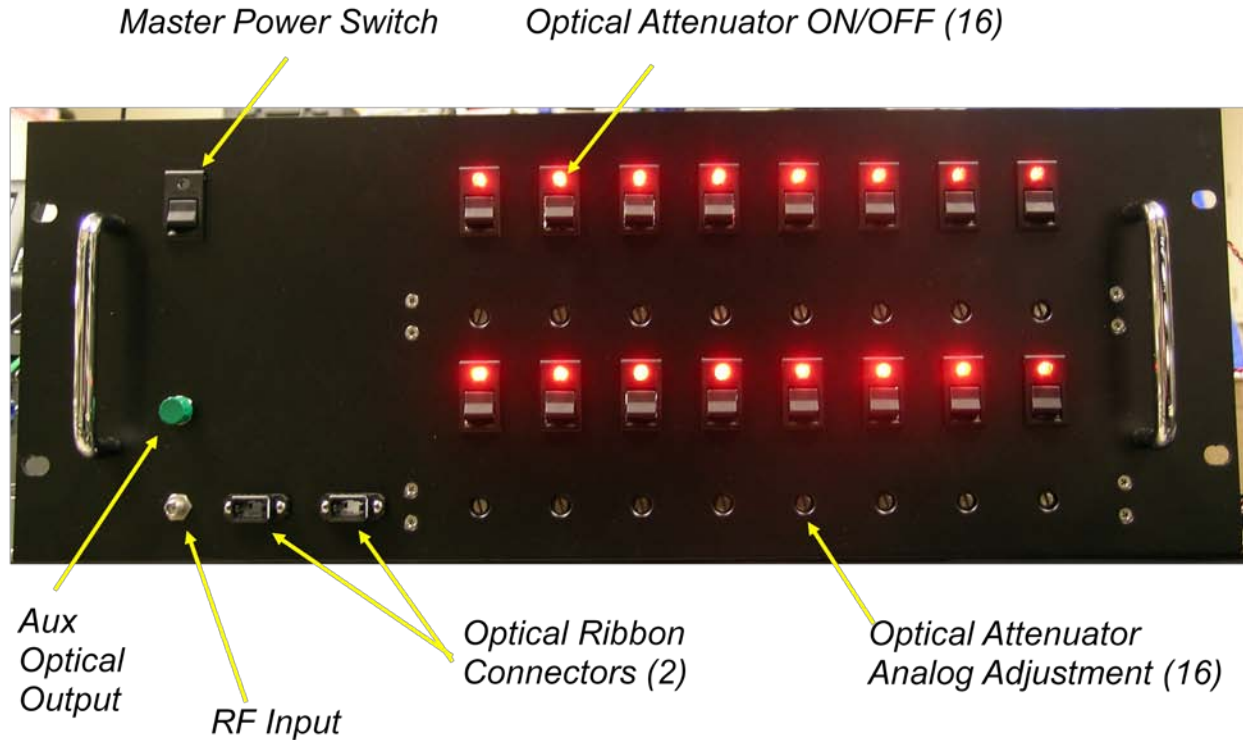


Figure 2-4: Front view photograph of the optical distribution network (ODN)

2.1 Characterization of Zero Bias Photodiodes

In the proposed architecture, the detectors are operated in a bias-free photo-voltaic mode to remove the need for a power distribution network embedded in the radome which avoids any mutual-coupling effects that will be caused by the additional bias distribution network. Normally, zero-bias photo-voltaic mode operation exhibits limited saturation output current and slow speed. However, recently, Discovery Semiconductor Technology demonstrated bias-free InGaAs PIN photodiodes that can be operated up to 30 GHz. In our current preliminary experiment, low-cost, more common and readily available InGaAs PIN photodiodes operating below 2.5 GHz were used. Zero-biased custom photodiode operation in radio-fiber systems has previously been demonstrated [10]. Commercial photodiodes are not typically operated in this zero-biased mode, thus the RF characteristics need to be studied to determine the properties and limitations of operation with zero-bias. A microscope image of the zero biased photodiode is shown in Figure 2-5.

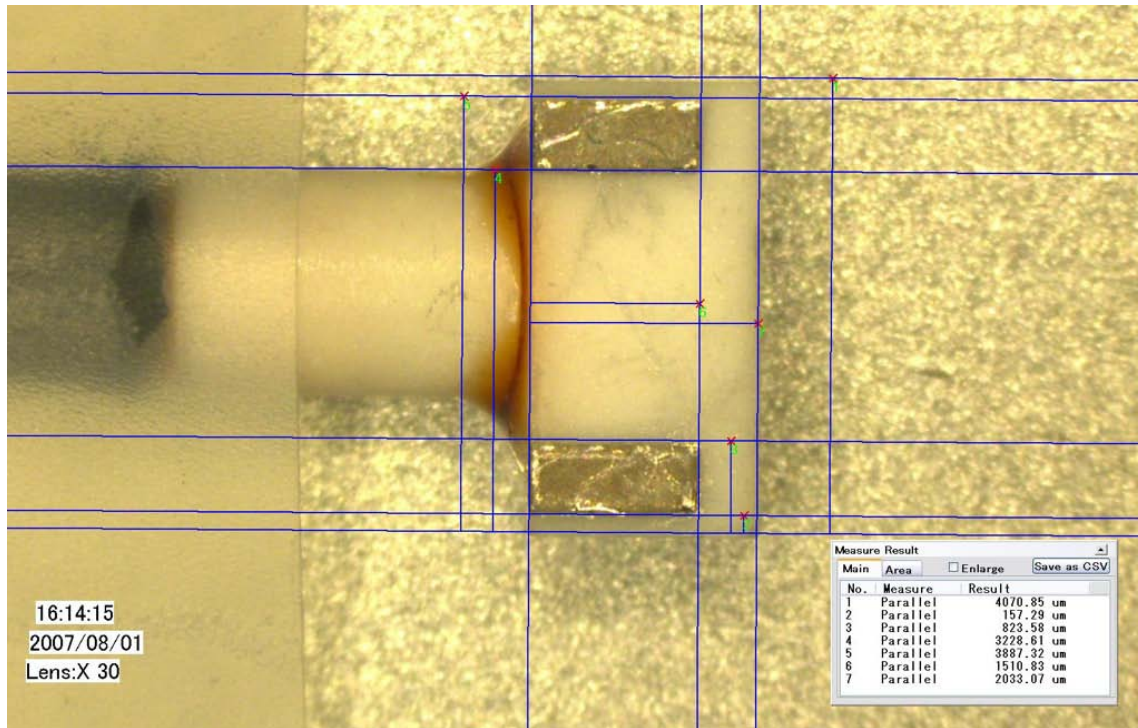


Figure 2-5: Microscope image with dimensions of the external packaging of zero bias photodiode

The fiber link supplying optical and RF signals to antennas used in the RF subsystem consists of a laser source externally modulated with a MZM. The modulated signal is amplified with an EDFA providing ample power to split into the required number of elements. Proper phase and amplitude matching of each fiber channel is achieved with common optical techniques, such as phase trimming and variable optical attenuators. The fibers terminate at array photodiodes that are directly connected to ESDAs. Intensity-modulated optical signals are demodulated by the photo detector, applied directly to the patch antennas, and received by the individual phased-array antenna elements for calibration.

The photodiodes in this work were first studied in unmodulated photovoltaic operation, and then examined with a modulated RF input to understand the response as a function of both DC optical power and RF frequencies. It is well known that operating PIN photodiodes at zero-bias degrades their overall performance. Compared to the reverse-biased state, the width of the depletion region is smaller under zero bias thus leading to higher junction capacitance and lower RC cut-off frequency. The shorter distance required for carrier transport is mitigated by lower drift velocity due to absence of the applied bias electric field. In addition to frequency response, some characteristics of interest in this study are the degradation of power saturation and optoelectronic power conversion in zero-bias operation.

2.1.1 Zero Bias Photodiodes – Setup

The photonic link for photodiode measurements is illustrated in Figure 2-6. The photodiodes under test were manufactured by Anadigics, Inc., in special ceramic sub-mount packages with single mode fiber pigtailed (PD070-001-720). Initial measurements were performed on a multiple fiber-pigtailed photodetectors, and it was found that the Anadigics devices to offer the best zero-bias performance were in a ceramic package. Optically, the same link architecture was used for the DC and RF measurements. The output of the semiconductor DFB laser was fed through a commercially-available MZM. Quadrature modulator bias was maintained by the use of a custom quadrature bias controller (QBC). The QBC compares the average optical power of the modulator output to the laser output and adjusts the MZM DC bias to maintain quadrature. If necessary, the QBC may be removed and quadrature can be maintained manually by monitoring the MZM output and adjusting the MZM bias voltage with an adjustable DC power supply. A variable optical attenuator (VOA) was used to vary optical power applied to the photodiode under test and the optical power was monitored from the 5% output of a 95/5 coupler by an optical power meter. The electrical output of the photodiode was measured using the SMA RF cable output a probe station.

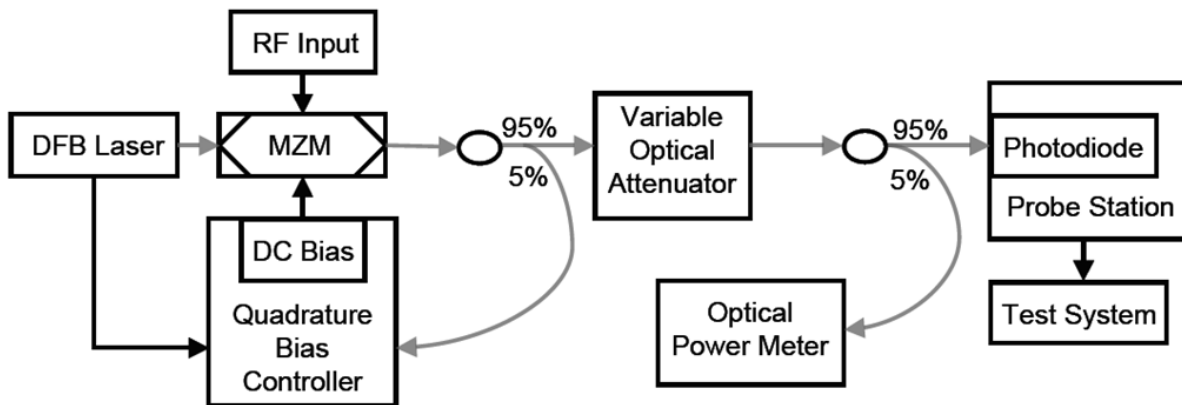


Figure 2-6: Photonic link used for photodiode measurements. The RF input method varied depending on the test at hand. The different test systems were designed for each measurement objective.

The photovoltaic measurements consist of 1) measuring the open-circuit voltage (V_{oc}), the short-circuit photocurrent (I_{sc}), and the $50\ \Omega$ -loaded photocurrent ($I_{50\Omega}$ with $R_L = 50\ \Omega$) as a function of input optical power, and 2) measuring the photodiode photocurrent versus the photodiode voltage, again as a function of input optical power. To measure photodiode voltage and current, the output from the photodiode was connected to the simple circuit shown in Figure 2-7a. The photodiode voltage, V_{PD} , was measured directly across the photodiode with a voltmeter and the photocurrent, V_I , was measured by monitoring the voltage across a $1\ \Omega$ resistor. R_L was a $1\ \text{M}\Omega$ potentiometer that was varied through its full range to change the photodiode voltage.

The RF measurements consist of measuring the RF output power with varying 1) applied bias

voltage, 2) optical input power, and 3) RF frequency. The first two RF measurements were obtained by applying a single 2 GHz tone with an RF source. The third measurement was conducted using a network analyzer varying the RF input frequency from 50 MHz to 8 GHz.

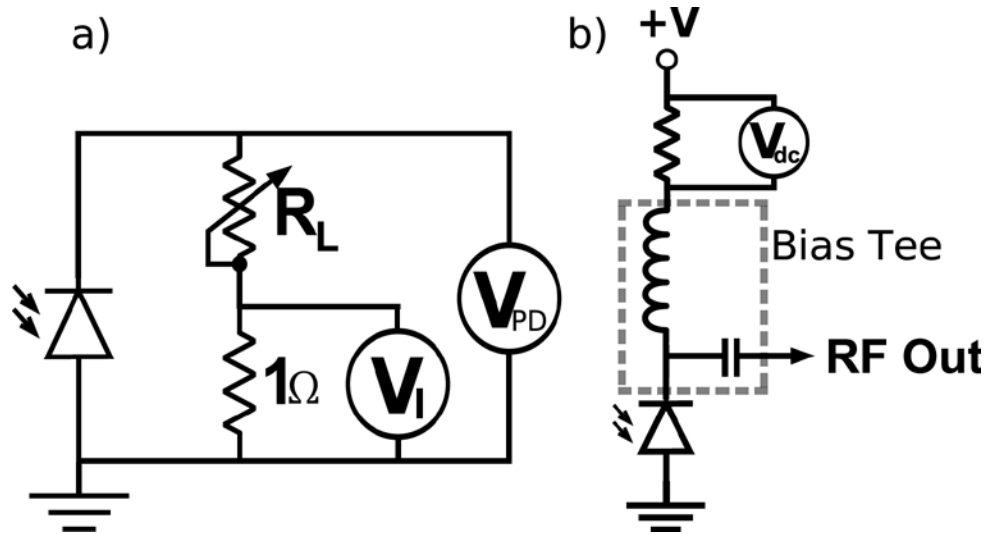


Figure 2-7: Photodiode measurement circuit diagrams. a) photovoltaic measurement circuit and b) RF measurement circuit with bias tee.

2.1.2 Zero Bias Photodiodes – Measurements

A critical aspect of the system is that the zero-biased photodiodes provide a means to remotely measure the calibration signals to the phased array radar interface without any electric wires which would create interference and system degradation. As a preliminary study of the project feasibility, we conducted extensive tests to test, analyze and verify the operational performance of zero-biased photodiodes.

2.1.2.1 Photovoltaic Measurements

Characterization of the photovoltaic properties of the photodiodes comprised measurements of the photocurrent and photodiode voltage for various levels of average optical power using the set-up shown in Fig. 2-6 and Fig. 2-7a.

Figure 2-8 shows the open-circuit voltage as a function of P_{opt} (Input optical power), and both the short-circuit photocurrent and the photocurrent with a series 50 ohm load, again as a function of P_{opt} . Figure 2-9 shows a family of $V-I$ curves, each for a specific P_{opt} value. These curves are parameterized by the load resistance R_L . That is, by manually adjusting the load resistance, various combinations of voltage and current are obtained.

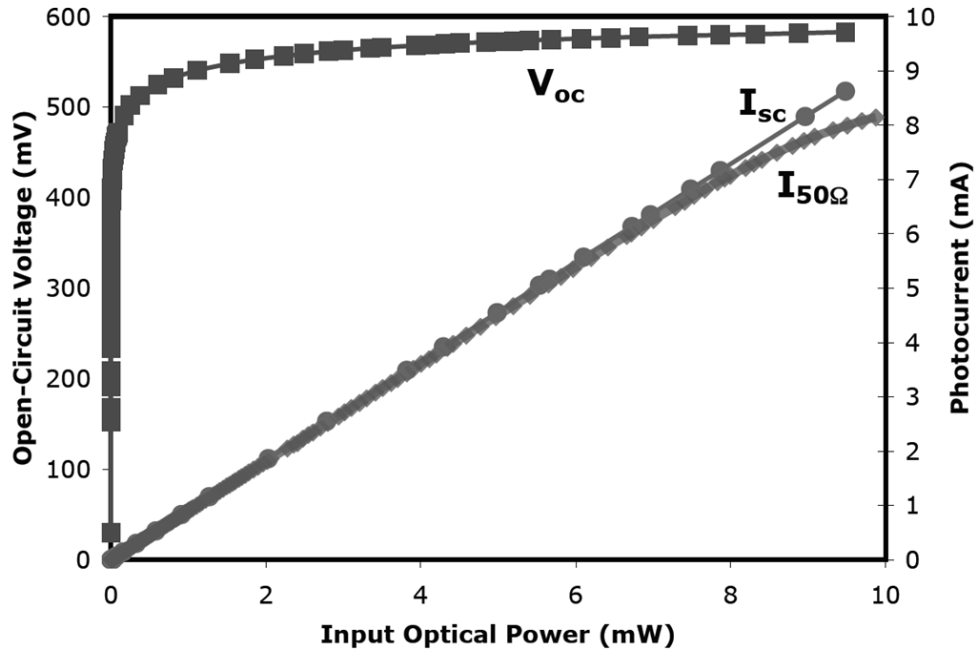


Figure 2-8: Open-circuit photodiode voltage, short-circuit photocurrent, and the 50 Ω load photocurrent as a function of input optical power.

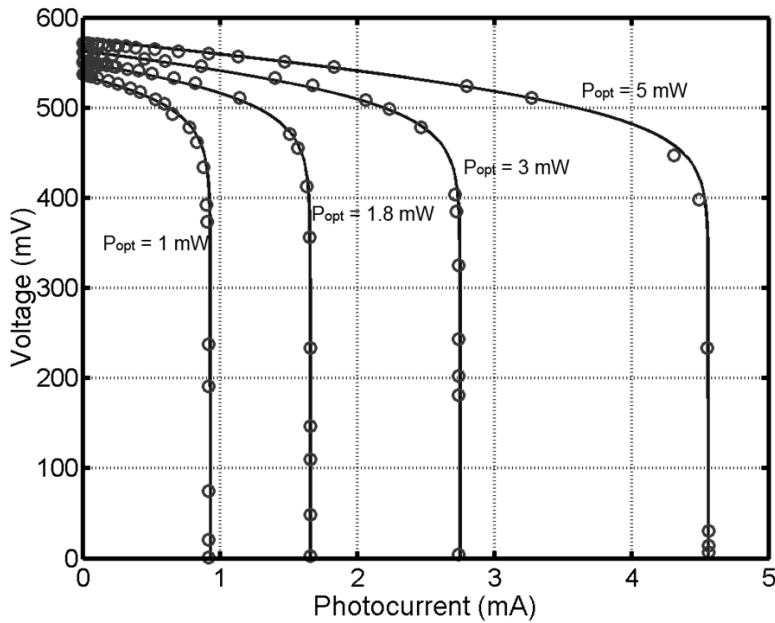


Figure 2-9: Voltage-current curves of photodiodes at zero-bias. The circles represent experimental data. The solid lines represent theory from (1) with $R_s = 10 \Omega$.

A good model for the photovoltaic response of the photodiode is given by the standard equation (2-1) [11]. Here V is the photodiode voltage and I is the current flowing through the external circuit, R_L and the 1Ω resistor, as defined in figure 2-7a, k is Boltzman's constant, T is the temperature, q is the charge on the electron, I_{sc} is the short-circuit photocurrent current, I_0 is the reverse saturation current and R_s is the series resistance internal to the photodiode.

$$V = \frac{kT}{q} \ln \left(1 + \frac{I_{sc} - I}{I_0} \right) - IR_s \quad (2-1)$$

In the linear regime, the short-circuit photocurrent is simply related to the optical power by $I_{sc} = \mathcal{R}P_{opt}$. Using the data in figure 2-8, a linear least-squares estimate yields the linear responsivity $\mathcal{R} = 0.91 \text{ A/W}$.

The open circuit voltage is found by setting $I = 0$ in (2-1).

$$V_{oc} = \frac{kT}{q} \ln \left(1 + \frac{\mathcal{R}P_{opt}}{I_0} \right) \quad (2-2)$$

By fitting visually the open-circuit voltage data to this equation we obtain an estimate of the reverse saturation current $I_0 = 0.8 \text{ pA}$.

Table 2-1: CURVE FITTING PARAMETERS FOR I-V CURVES SHOWN IN FIGURE 2-9.

$$\mathcal{R} = 0.91 \text{ A/W}, I_0 = 0.8 \text{ pA}, R_s = 10 \Omega$$

| | | | | | |
|-------------------|-----------|------|------|------|------|
| Nominal (mW) | P_{opt} | 5.0 | 3.0 | 1.8 | 1.0 |
| Curve-fit (mW) | P_{opt} | 5.01 | 3.02 | 1.82 | 1.02 |

The internal series resistance R_s can be obtained by curve-fitting the full (2-1) to the data in figure 2-9. Best visual fits were obtained using the parameter values shown in Table 2-1. In each case, the current value in the limit of zero load resistance is just I_{sc} . We are clearly in the regime where $\mathcal{R}P_{opt} \gg I_0$, and so to a good approximation the voltage in the open-circuit limit is that defined in (2-3). That is, for fixed temperature and input optical power, the open-circuit voltage is determined entirely by the ratio of the responsivity to the reverse saturation current.

$$V_{oc} \approx \frac{kT}{q} \ln \left(\frac{\mathcal{R}P_{opt}}{I_0} \right) \quad (2-3)$$

The data in figure 2-9 were obtained by adjusting R_L to change the photodiode voltage and we chose to plot V as a function of I to facilitate comparison with (2-1). In some cases it is more meaningful to treat V as the independent variable in which case it is necessary to invert (2-1) to express I as a function of V , $I=f(V)$. This can be done using the Lambert W function.

2.1.2.2 RF Power Measurements

The RF response for a single tone RF signal at 2 GHz is measured as a function of both bias voltage and input optical power. A 2 GHz RF tone is injected into the MZM with an Agilent vector signal generator. A Hewlett-Packard RF power meter is connected to the photodiode output through a bias tee, seen in figure 2-7b, to measure the RF output. This output can be checked for consistency using a spectrum analyzer. The spectrum analyzer is also useful to examine the harmonic frequencies created during modulation and detection. A tunable RF filter is used on the input to the MZM to reduce harmonic content from the signal generator. In addition, low amplitude RF inputs are used to minimize MZM nonlinearities.

RF compression of the photodiode response occurs in the low-bias regime as can be seen in figure 2-10. The severity of the RF compression at low applied bias increases with optical power. At 1 mW, the zero-biased photodiode has approximately 3 dB of RF compression; whereas at 5 mW, the RF compression has increased to 11 dB. Of course, increasing the bias voltage relieves the compression and results in the expected difference in RF output power between optical input power curves. However, it is evident that a significant amount of RF power is available even at zero bias.

Figure 2-11 shows the RF output power as a function of optical power level for three different values of RF modulation power applied to the MZM. The roll-off in response in these devices above approximately 2 mW is most likely the result of forward biasing of the junction induced by the input optical power. Hence, this plot reveals an operating point optimized for RF output power level near 1 mW input optical power. It should be noted that this optimum regime has been established for the case of the diode driving a 50 Ω load. For the application mentioned earlier, namely, a photodiode driving a small patch antenna, the optimum operating conditions in a given RF frequency range may be different.

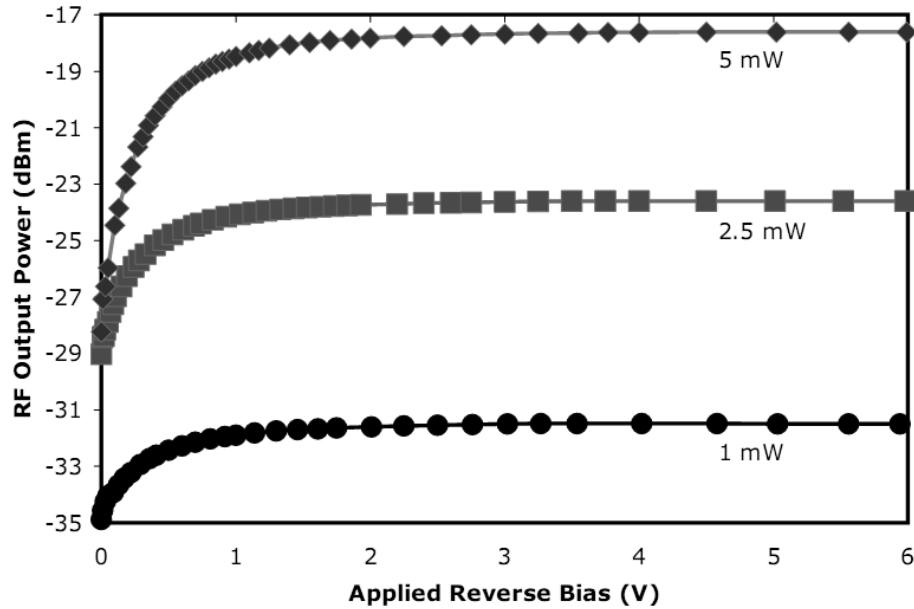


Figure 2-10: PD RF output power at 2 GHz as a function of reverse bias voltage for various optical power levels.

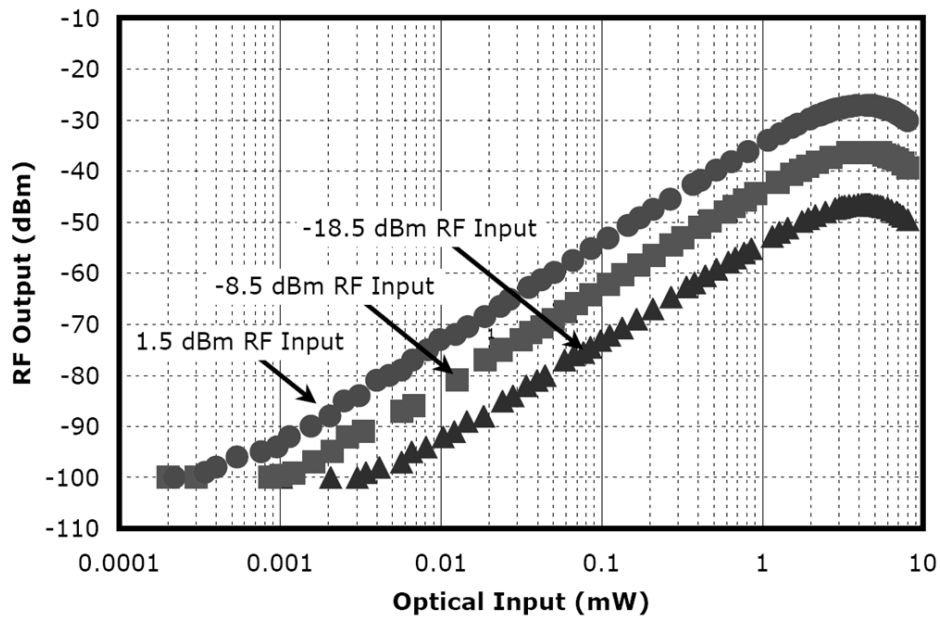


Figure 2-11: RF output power from zero-bias photodiode as a function of input optical power with 2 GHz RF input to the MZM at -18.5 , -8.5 , and 1.5 dBm.

In Figure 2-8, the photocurrent with a 50Ω load was shown. This measurement is used here to calculate the semi-theoretical RF output power for increasing optical input power. The calculated RF output power is then compared to the measured output power of Fig. 2-11. To make this calculation we start with the RF gain for small input signals as defined in (2-4) [12].

$$G_{rf} \equiv \frac{I_{dc}^2}{V_{\pi}^2} \pi^2 Z_{in} Z_{out} \quad (2-4)$$

In (2-4), I_{dc} is the detector photocurrent, Z_{in} is the input impedance seen by the RF source, Z_{out} is the output impedance seen by the photodiode, and V_{π} is the modulator half-wave voltage. Since the gain is the ratio of output power to the input power, the RF output power can be written as (2-5), where $P_{rf,in}$ is the RF power supplied by the RF source.

$$P_{rf,out} = \frac{I_{dc}^2}{V_{\pi}^2} \pi^2 Z_{in} Z_{out} P_{rf,in} \quad (2-5)$$

In general, the RF response should be proportional to the slope of the DC response. With the unbiased photodiode and a 50 Ω load, Figure 2-8 shows that the detector photocurrent is no longer a linear function of the input optical power at high optical powers and, hence, the RF power is no longer linearly proportional to input optical power at high optical power.

The analytic expression for $I_{50\Omega}$,

$$I_{50\Omega} = I_{dc} - I_0 \left(e^{qV_L/kT} - 1 \right) \quad (2-6)$$

depends on multiple factors related to the intrinsic properties of the diode as well as the temperature of the junction (T) which may also be a function of P_{opt} . Therefore, this function is not easily modeled. To simplify, instead, a polynomial fit to the $I_{50\Omega}$ curve in Figure 2-8 is used to calculate the instantaneous slope for a given P_{opt} .

For the case of each input power, the instantaneous slope of the $I_{50\Omega}$ curve in Figure 2-8 is multiplied by the input power to obtain the expected detector photocurrent.

$$I_{dc}(P'_{opt}) = \left. \frac{\partial I_{50\Omega}}{\partial P_{opt}} \right|_{P'_{opt}} P'_{opt} \quad (2-7)$$

The RF output power can be calculated using (2-8) and is plotted in Figure 2-12. The decrease in RF response above 1 mW (see inset in Fig. 2-12) cannot solely be due to photodiode loading since $I_{50\Omega}$ is a measure of loading. It should be noted that the inset plot of Figure 2-12 shows the difference in the RF output power predicted from $I_{50\Omega}$ and the measured power in Figure 2-11. Whatever the mechanism, the operating limitations are clear. The RF response will maximize at around 4 mW but operation at a more conservative value of 1-2 mW is probably warranted.

$$P_{rf,out} = \left(\left. \frac{\partial I_{50\Omega}}{\partial P_{opt}} \right|_{P'_{opt}} P'_{opt} \right)^2 \frac{\pi^2 Z_{in} Z_{out} P_{rf,in}}{V_{\pi}^2} \quad (2-8)$$

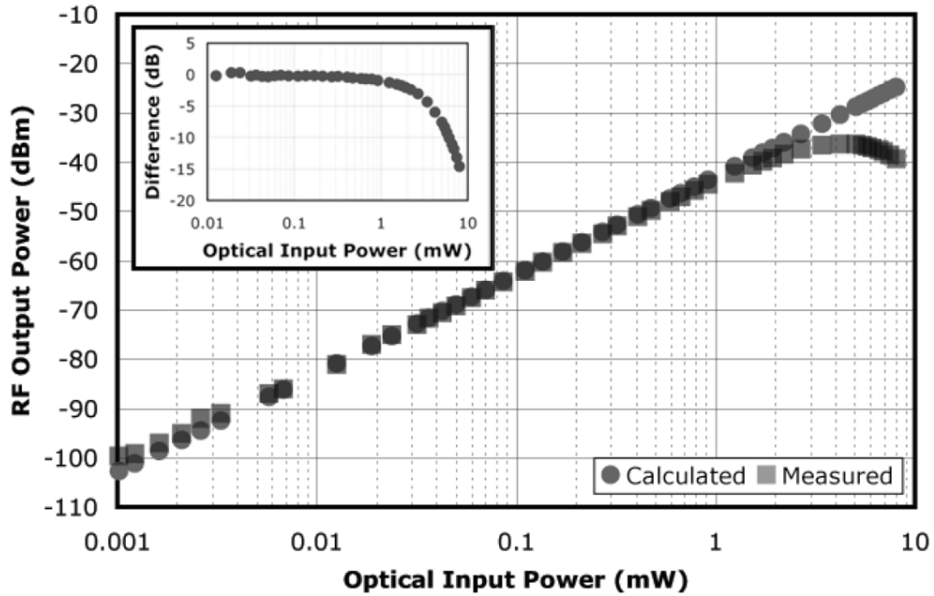


Figure 2-12: The measured RF output power as a function of optical input power and the RF output power calculated from the slope of the $I_{50\Omega}$ curve in Fig. 4. Inset shows the difference in the RF output power predicted from $I_{50\Omega}$ and the measured power in Fig. 2-11.

The frequency response of the link including the photodiode and modulator is obtained using an Agilent network analyzer. The S_{21} response is measured from 50 MHz to 8 GHz at increasing bias voltages from 0 to 5 V. Again, the output of the photodiode goes through a bias tee for RF output and DC input. The frequency response of the photodetectors is shown in Fig. 2-13.

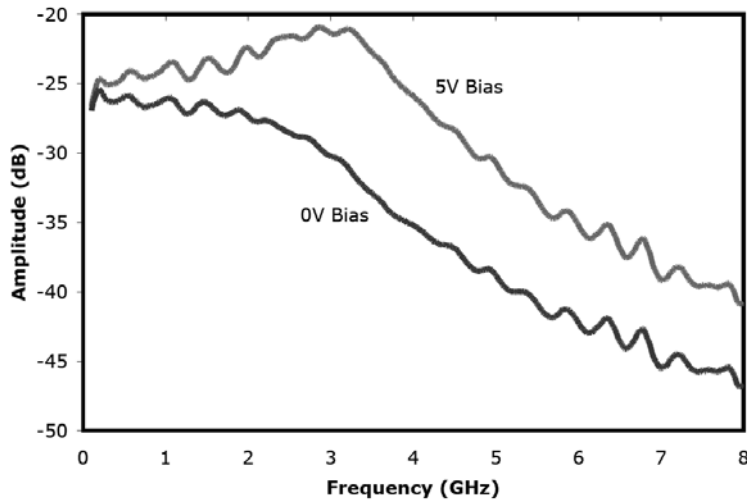


Figure 2-13: Frequency response of the photodiode at 0 and 5 V reverse bias from 50 MHz to 8 GHz. An optical input power of 2.5 mW and RF input power of 5 dBm is used.

2.1.2.3 RF Distortion Measurements

Harmonic distortion measurements were made using a heterodyne laser setup [13-15]. Two

phase-locked Nd:YAG lasers operating at wavelengths λ_1 and λ_2 (Figure 2-14) beat together on the photodetector to supply a pure RF tone. A third laser, λ_3 , operated at a wavelength sufficiently far from λ_1 and λ_2 so as to not create any beat terms in the frequency range of interest, is used to maintain constant total optical power on the photodiode as the strength of the beat signal is varied. In this way, harmonic terms are attributable entirely to the photodiode and not to the signal source. We chose 1 mA of DC photocurrent since it is well below the region where the RF power response deteriorates (Fig. 2-11). We chose a tone at 1GHz to ensure the harmonic content would be well within the bandwidth of the photodiode (Fig. 2-13).

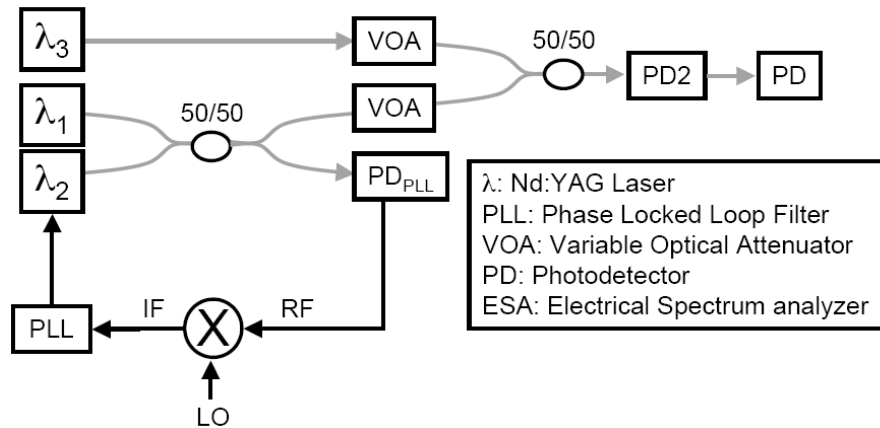


Figure 2-14: Photodiode harmonic distortion phase locked loop measurement setup.

This heterodyne setup uses three Nd:YAG lasers operating in the 1319 nm wavelength range, not at the system wavelength of 1550 nm. However, we are concerned with the nonlinearities of the photodiode at RF frequency and believe the behavior is similar at both optical wavelengths. The results are shown in Figure 2-15 and 2-16. Figure 2-15 shows the harmonic content as a function of bias voltage. Due to space charge effects, harmonic distortion improves with increasing bias voltage [16]. At the zero-bias point the second harmonic is approximately 40 dB down from the fundamental and the third harmonic is over 50 dB down from the fundamental. The measured second- and third-order output intercept points (OIP2 and OIP3), in Figure 2-16, also improve with increasing reverse bias voltage. At 1 mA DC photocurrent and zero-bias, OIP2 is approximately 21 dBm whereas OIP3 is 9 dBm. This represents a rather stiff RF penalty to be paid for operation at zero bias. However, it can easily be tolerated for sub-octave systems employing a single frequency RF tone for calibration.

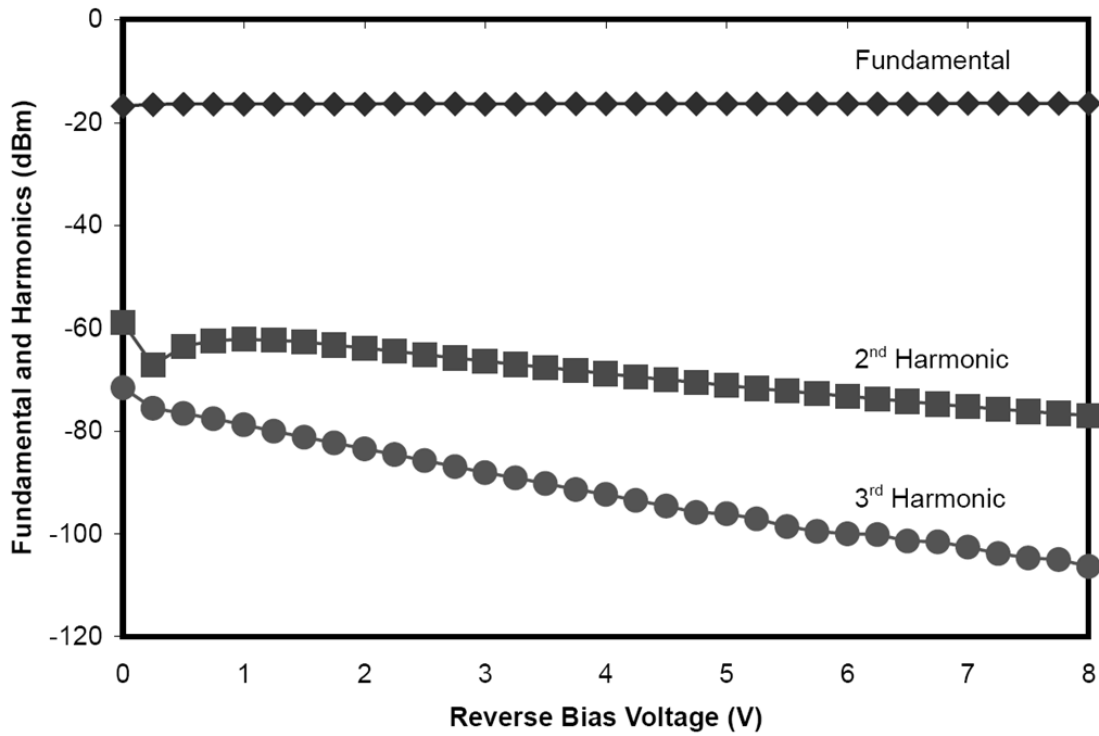


Figure 2-15: Fundamental and harmonic response of photodiodes with an incident optical input at 1 GHz absent any harmonic content by means of a heterodyned laser setup. The heterodyne system is designed so the DC photocurrent remains constant, in this case at 1 mA.

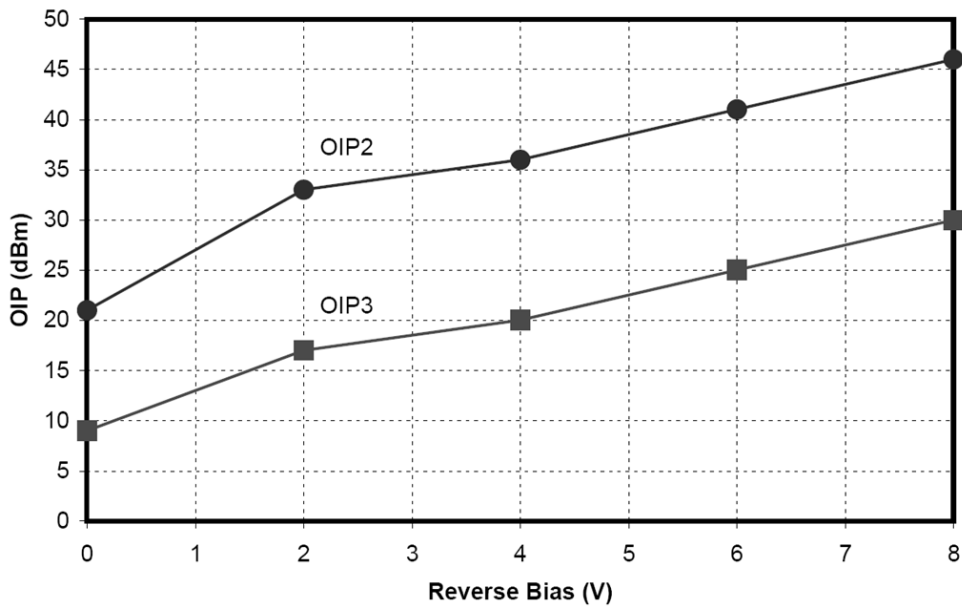


Figure 2-16: Output intercept point of the second and third harmonic (OIP2 and OIP3 respectively) as a function of applied reverse bias. 1 GHz input tone with 1 mA DC photocurrent. The circles represent the OIP2 and the squares represent the OIP3.

2.2 Hardware and Components

Output from a distributed feedback (DFB) laser (JDSU, model CQF938, high power 1550nm CW laser with PM fiber pigtailed) operating at 1.55 μm is modulated by a lithium niobate modulator (JDSU, model APE AM-150, analog intensity modulator), and the modulated signal is detected by a photodiode. The photodiode is a fiber-pigtailed InGaAs PIN diode (GPD-IR'S model GAP60PTSFCPC and Anadigics' model PD70-HL1-120, 70 μm diameter) that is operated in a bias-free mode (photo-voltaic mode) to minimize electromagnetic interference (EMI) effects. In general, the photovoltaic mode provides low saturation current and low speed, as described previously. However, when the incoming light is weak (typically less than 0 dBm), the zero-bias mode exhibits behavior similar to that of the non-zero bias mode in terms of L-I (light vs. current) curve response. The current generated by the photodiode drives the ESDA in the RF subsystem.

Inside the fiber or waveguides, different wavelengths of light propagate at different speeds. As a result, a wideband signal at the input becomes smeared at the output. The amount of time delay Δt is proportional to the length of the waveguide (L) and the spectral linewidth of the laser source ($\Delta\lambda$) and is given by $\Delta t = D_\lambda \cdot L \cdot \Delta\lambda$, where D_λ is the dispersion coefficient, which is 17 ps/nm-km for standard SMF-28 single-mode fibers. A single mode PLC is expected to have a similar amount of dispersion. The spectral linewidth of a DFB laser modulated at 20 GHz is approximately 0.16 nm. Therefore, the total amount of dispersion over a length of 2 m is 5.44×10^{-3} ps. This is only 1% of the required timing resolution of 0.5 ps.

The center wavelength of a DFB laser drifts at a rate of 0.1 nm/ $^\circ\text{C}$. Also, the dispersion coefficient of an SMF-28 fiber varies as 0.001 ps/($^\circ\text{C}$ -nm-km). For a temperature variation of 100 $^\circ\text{C}$, total time delay becomes 0.34 ps, which is less than the required timing resolution of 0.5 ps. Further, a dispersion-shifted fiber or a different wavelength (1310 nm) can be used for even lower dispersion. Therefore, dispersion is not an issue with our architecture.

The performance of the in-line, voltage-controlled variable optical attenuators are shown in the figures below. Figure 2-18 shows it is possible to get 35 to 45 dB of attenuation when applying 1.5 to 1.6 volts respectively, while figure 2-19 shows optical stability over time after the initial warm up period. Figure 2-20 shows the analog adjustment range in optical power for all 16 VOAs where maximum attenuation values may differ as much as 10 dB due to the large negative slope shown at the tail end of figure 2-18.

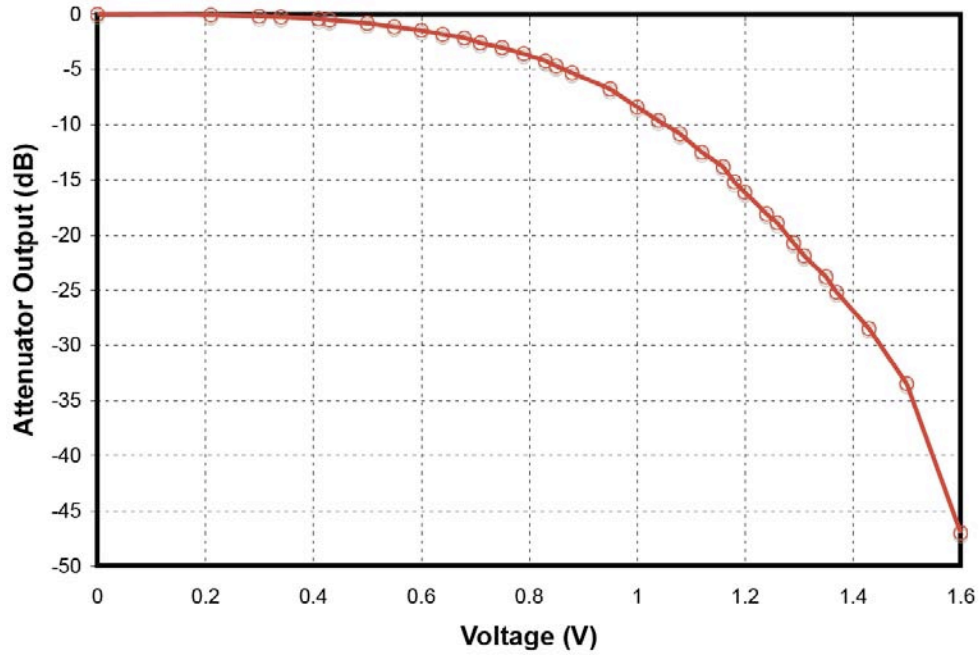


Figure 2-17: Attenuation vs. applied electric voltage for variable optical attenuators

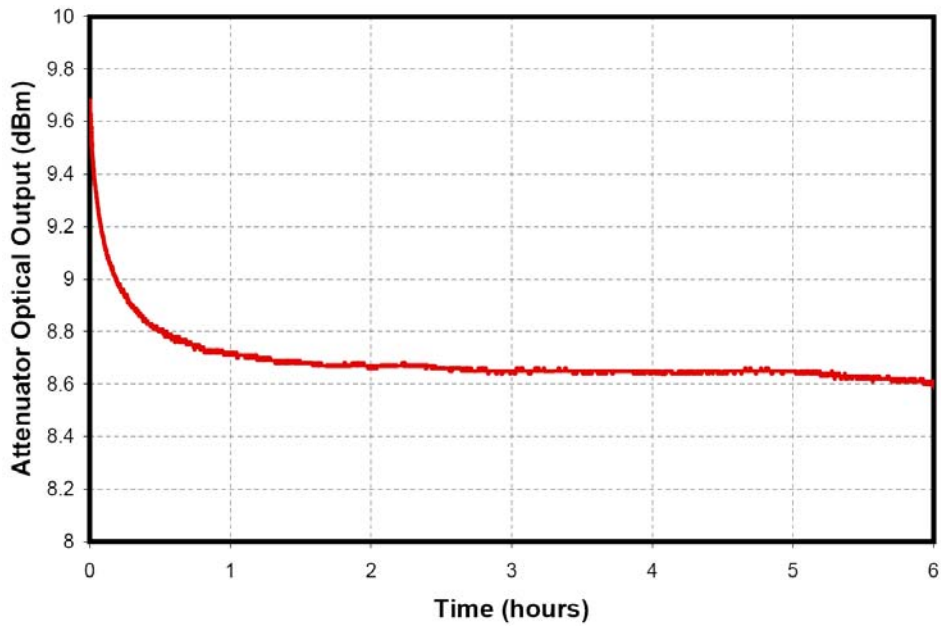


Figure 2-18: Variable optical attenuator stability over time

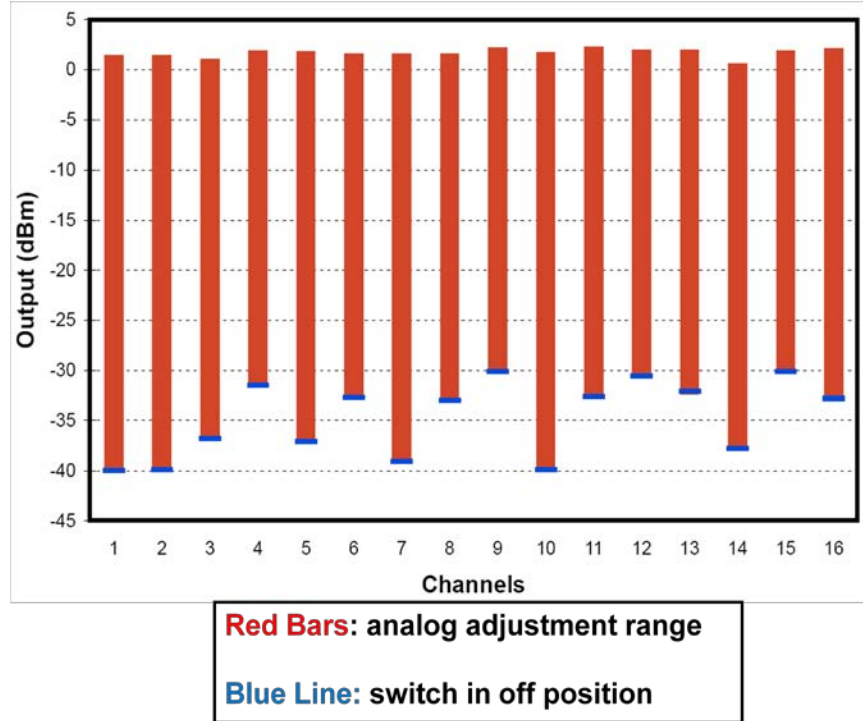


Figure 2-19: Bar graph displaying the individual output optical power range for 16 VOA's

2.3 Time Trimming

Traditionally, optical fibers have been extensively used for timing signal distribution for various applications. However, in microwave calibration applications that require precise timing control, the use of optical fibers raises two main issues - timing resolution and hardware complexity. For example, a 20 GHz signal requires 0.5ps timing resolution that corresponds to an optical fiber length of 100 microns. It is difficult to cut a fiber to a desired length to within an error of 1 mm which is much longer than 100 microns. Although, the resolution can be improved by a repeated trial-and-error polishing procedure, it is extremely time-consuming. Furthermore, fiber lengths can be changed by external conditions such as temperature and stretch. Therefore, it is difficult to maintain a large number of long fibers with a high degree of timing precision (<0.5ps), as is required in our application. More importantly, it is challenging to operate a fiber-based timing network in the matrix addressing mode that requires a precise coupling of light from two fibers onto a single photodiode while maintaining precise relative positioning relationship between the fibers and the photodiode. Therefore, fiber-based timing network must be operated in an individual addressing mode. This requires a prohibitively large number (N^2) of fibers, and amplitude and delay controls for an $N \times N$ phased array. Furthermore, such a large number of fibers must be maintained precisely against adverse environmental conditions. In this regard, a planar lightwave circuit PLC has clear advantages over fibers for microwave calibration

purposes, especially at high frequency (due to precise timing control) and for a large number of elements (due to matrix addressing).

The dimensions of a PLC can be very precisely defined with sub-micron resolution due to the micro-lithographic process. This translates to a timing resolution of 0.005 ps, or 10^{-4} of the period at 20 GHz. The change in optical path length (OPL) of an optical waveguide (including both optical fibers and PLCs) due to temperature variation is given by (2-9).

$$\Delta(OPL) = nL \left(\frac{1}{n} \frac{\partial n}{\partial T} + \frac{1}{L} \frac{\partial L}{\partial T} \right) \Delta T \quad (2-9)$$

where n , L and ΔT are the refractive index of the waveguide material, geometrical path length and the increment in temperature, respectively. The first term on the right side of the equation refers to the thermo-optic effect, and the second term refers to the coefficient of thermal expansion (CTE). For SiO_2 (the waveguide material for optical fibers and PLCs), the combined number in the parenthesis becomes $7.6 \times 10^{-6}/^\circ\text{C}$. For a 24 element-array and the temperature variation of 20°C (during the calibration period of approximately one hour), the maximum time delay due to the combined dispersion and temperature effects becomes 3.5×10^{-3} of the period. Therefore, the PLC can be considered precise enough to be used as a reference for calibration.

3 RF SUBSYSTEMS

Multiple RF subsystems were developed to demonstrate the performance and stability of the photonic-based calibration system. The primary subsystem consists of a band pass frequency selective surface (FSS) with integrated electrically short dipole antennas (ESDAs). This section of the report includes the design of the FSS, integration of the photonic subsystems into the FSS, and characterization of the FSS RF performance. In addition to design of the FSS, a broadband dipole array was built to serve as a test array for the calibration technique. The array consists of tightly-coupled microstrip dipole elements fed with a dual Marchand balun. The design and performance of the array are discussed in this section of the report. The architecture of the photonic calibration system is provided in Figure 3-1.

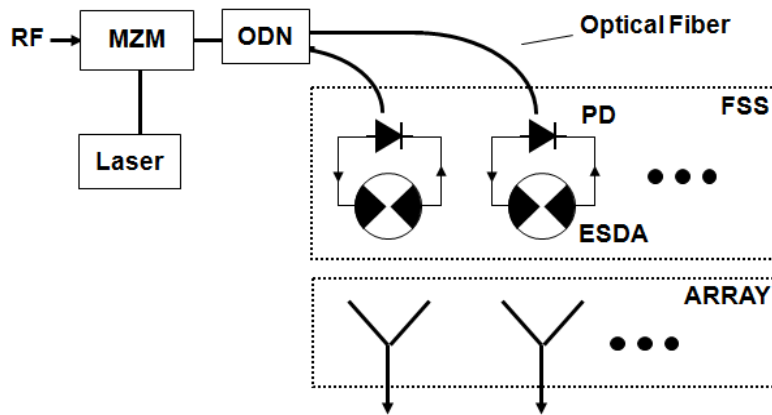


Figure 3-1: Architecture for phased-array calibrator employing an array of zero-biased photodiodes (PD) each driving an electrically short dipole (ESDA). Each PD receives RF-modulated light from a single-mode optical fiber through an optical distribution network (ODN).

3.1 Design and Performance of Electrically Short Dipole Antenna (ESDA)

The optical calibration approach illustrated in Figure 3-1 requires the installation of a zero-biased photodiode (PD) and accompanying ESDA above each element in the antenna array. Within the optical distribution network (ODN), the RF modulated signal is optically amplified and then distributed to an ESDA located adjacent to each element in the phased array to be calibrated. Each channel of the photonic calibration network allows static adjustment over both the amplitude and phase. After photodetection, the RF signal is placed across the ESDA antenna located at each unit cell in the FSS. The RF signal excites currents on the ESDA, and the dipole will transmit the calibration signal to the corresponding antenna element.

A RF modulated signal is placed across the photodiode exciting currents on an ESDA, and the ESDA transmit the calibration signal the corresponding antenna element. In order to place the optical diode at the desired location (centered above each antenna element), the diodes are mounted in a dipole-like probe. The shape of the electrically short dipole antenna (ESDA) is

shown in Figure 3-2. The location of the photodiode integration is circled for clarity. The circular shape of the ESDA was selected to facilitate integration with a frequency selective surface (FSS) that is described in a later section of this report.

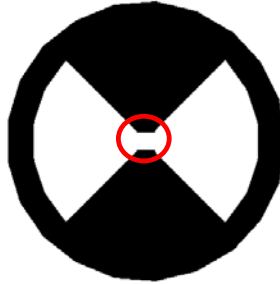


Figure 3-2: Illustration of the shape for an electrically short dipole antenna (ESDA) with location of integrated photodiode circled

3.1.1 Induced Voltage Simulations

The voltage induced across the probe was studied via simulations in CST Microwave Studio [17]. The probe was placed inside of an S-Band waveguide with a diode across the gap as shown in Figure 3-3. The properties assigned to the diode are provided in Table 3-1. A 1-Watt TE₁₀ waveguide mode was transmitted through the waveguide, and the induced voltage across the diode was studied. The simulated field distribution in the plane containing the probe is shown in Figure 3-4; this distribution indicates that the field is concentrated across the gap of the probe as anticipated. The resulting induced voltage across the diode is plotted in Figure 3-5. The shape and gap of the ESDA were optimized to maximize the voltage induced across the diode.

Table 3-1: Diode Parameters for Simulation

| Parameter | Value |
|------------------------------------------|----------------------|
| I₀ (Dark Current) | 0.05 nA |
| G_s (Shunt Conductance) | 10 ⁻⁹ mho |
| R (Series Resistance) | 10 Ω |
| C | 0.4pF |

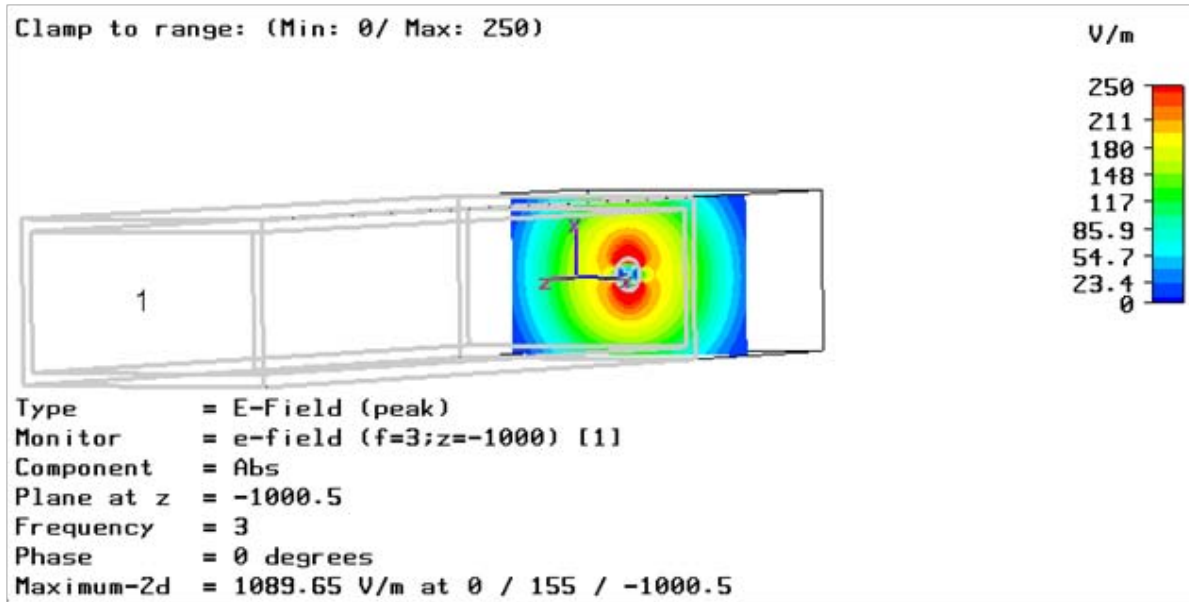


Figure 3-3: Simulation model used to study the voltage induced on a diode placed across the gap of an electrically short dipole antenna (ESDA)

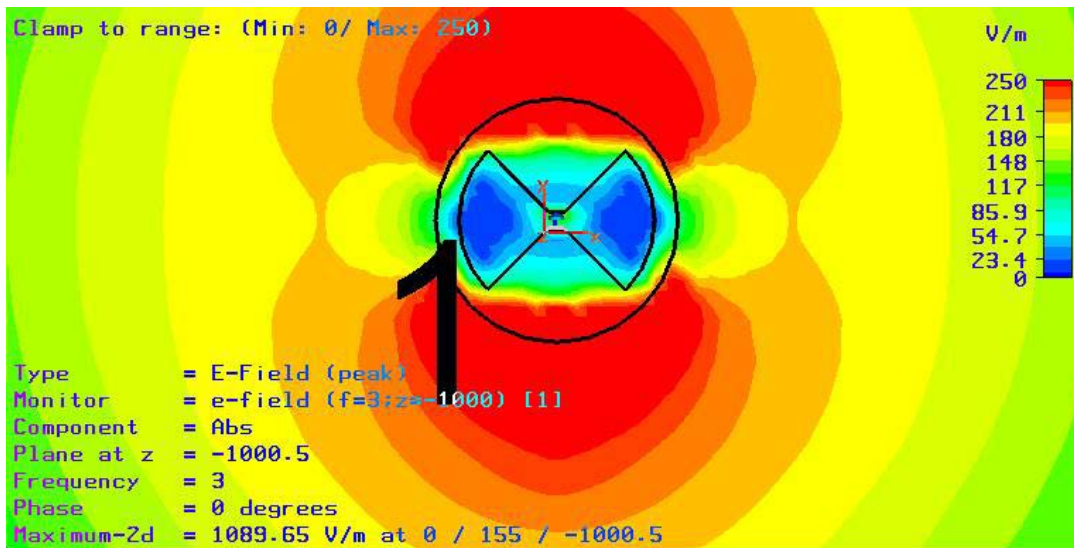


Figure 3-4: Simulated Electric Field Distribution in S-band Waveguide Containing an electrically short dipole antenna with a diode placed across the gap

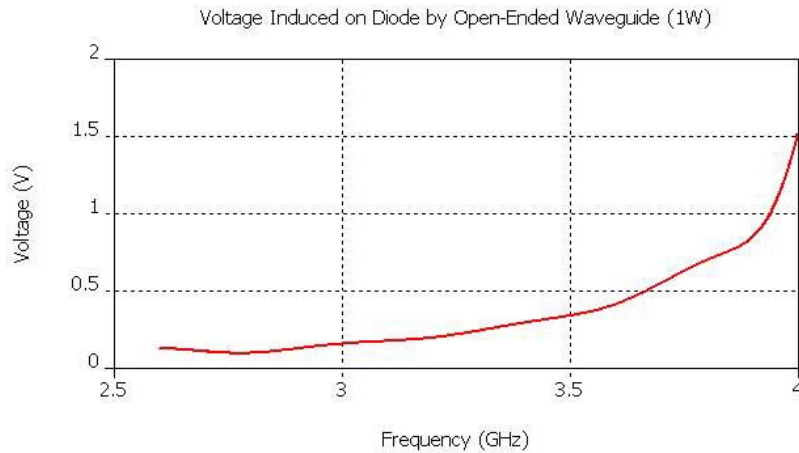
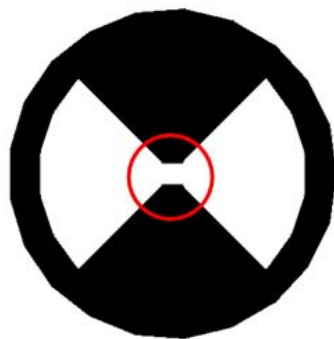


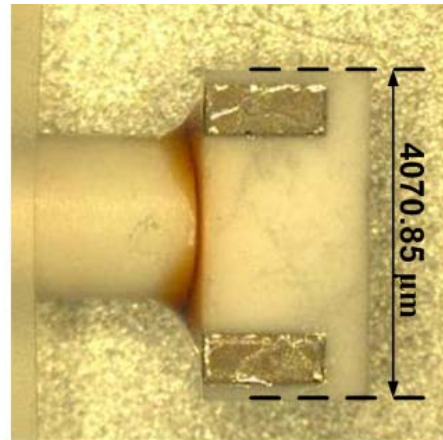
Figure 3-5: Simulated voltage across a diode placed in the gap of an electrically short dipole antenna (ESDA) resulting from a 1W TE₁₀ waveguide mode

3.1.2 Integration of Photodiode into ESDA

The calibration system will include a FSS containing photodiodes integrated into ESDAs. The conducting grids for the FSS will be etched onto a microwave substrate. Subsequently, the ESDA and accompanying photodiodes will be integrated together in a printed circuit board (PCB) design. The shape of the ESDA is shown in Figure 3-6(a), and the gap where the diode will be located is circled for clarity. A photograph of the photodiode used in this design is provided in Figure 3(b). The photodiode contains a pigtailed single mode fiber and has a photosensitive region 70 μm in diameter with a responsivity of 0.91 mA/mW.



(a) Shape of the electrically short dipole antenna (ESDA)



(b) External electrical connection pads of the zero-bias photodiode

Figure 3-6: (a) Shape of the electrically short dipole antenna (ESDA) used for integrating photodiodes into a frequency selective surface, (b) Photograph of external electrical connection pads of the zero-bias photodiode (Anadigics PN: PD070-001-720) with responsivity of 0.91mA/mW

In the PCB realization, the photodiode will be placed on the side of the microwave substrate opposing that containing the ESDA. This is done to allow the optical fibers to pass beneath the PCB, and thus minimize their interaction with the ESDA. Conducting solder pads are printed on the bottom side of the microwave substrate and plated through holes are added to provide electrical continuity between the printed diode and the solder pads. The photodiode is installed across the solder pads on the back side of the dielectric substrate. A detailed drawing showing the ESDA, solder pads, plated through holes, and photodiode is provided in Figure 3-7. In this figure, one side of the ESDA is removed for clarity.

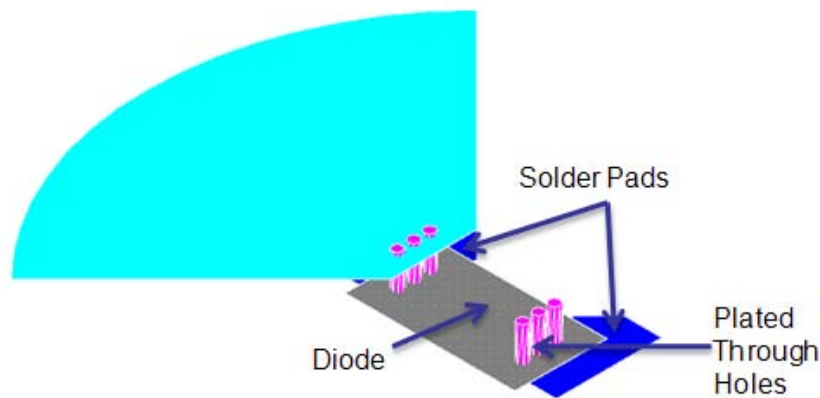


Figure 3-7: Detailed drawing showing the integration of the photodiode with the dipole probe

3.2 Design and Performance of a Bandpass Frequency Selective Surface with Integrated Photodiodes

A frequency selective surface (FSS) provides minimal attenuation in the passband while becoming increasingly opaque outside of the pass band. This type of structure is often used in the design of a hybrid radome consisting of FSS layers sandwiched between dielectric layers; the goal of the hybrid radome is to reduce the out of band radar cross section (RCS) of an antenna. At frequencies where the FSS is opaque, the incident signal is reflected back in the bi-static direction [18]. At frequencies where the radome appears transparent, minimal RCS improvements are seen. However, if the pass band of the hybrid radome coincides with the operational frequency band of the phased array, the energy incident on the array can be received with minimal attenuation. For this demonstration, a FSS with a pass band covering 2.5-3.5 GHz was designed.

In FSS designs, conducting grids appear inductive to incident waves while arrays of conducting patches appear capacitive. In a design proposed by Wahid and Morris [19], a conducting grid and an array of conducting patches are superimposed to result in a band pass structure. The design used in this demonstration is based on the ideas and concepts from Wahid and Morris

[19]. The unit cell for the band pass FSS shown in Figure 3-8(a), is a square with side length of 4.32cm. The conducting grid consists of a rectangular grid with 0.24cm thickness, and each corner has a 90-degree arc with a 1.27cm radius. The center of the unit cell consists of a 1.27cm radius circular patch that will serve as the capacitive component. The conducting pattern is printed on RO4350 substrates ($\epsilon_r=3.48$, $\tan\delta=0.04$, $h=0.076\text{cm}$) that are present above and below a 1.2" thick honeycomb core. The dielectric profile of the FSS unit cell is shown in Figure 3-8(b).

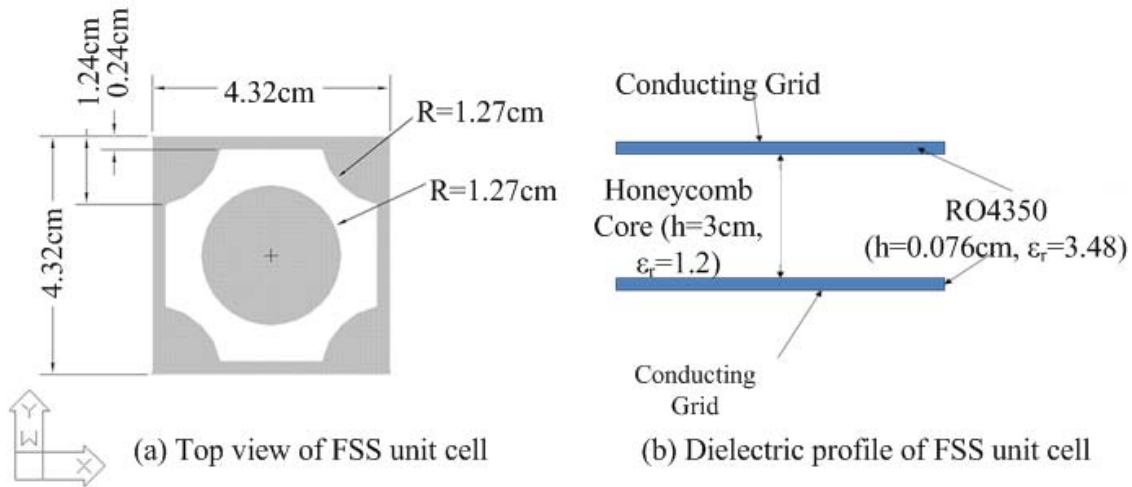


Figure 3-8: Top view (a) and dielectric profile (b) of a frequency selective surface (FSS) with 2.5-2.5GHz passband

The center of the FSS unit cell is modified to include the ESDA and accompanying photodiode described in the section 3.1. Conducting solder pads are printed on the bottom side of the microwave substrate and plated through holes are added to provide electrical continuity between the printed diode and the solder pads. The photodiode is installed across the solder pads on the back side of the dielectric substrate. The unit cell of the FSS with integrated optical calibration system is detailed in Figure 3-9. The conducting pattern is printed on RO4350 substrates ($\epsilon_r=3.48$, $\tan\delta=0.04$, $h=0.03\text{''}$) that are present above and below a 3cm thick honeycomb core ($\epsilon_r=1.2$). The dielectric profile is identical to that for the design shown in Figure 3-8(b). The bandpass for the FSS covers the 2.5 – 3.5 GHz operational bandwidth of the phased array.

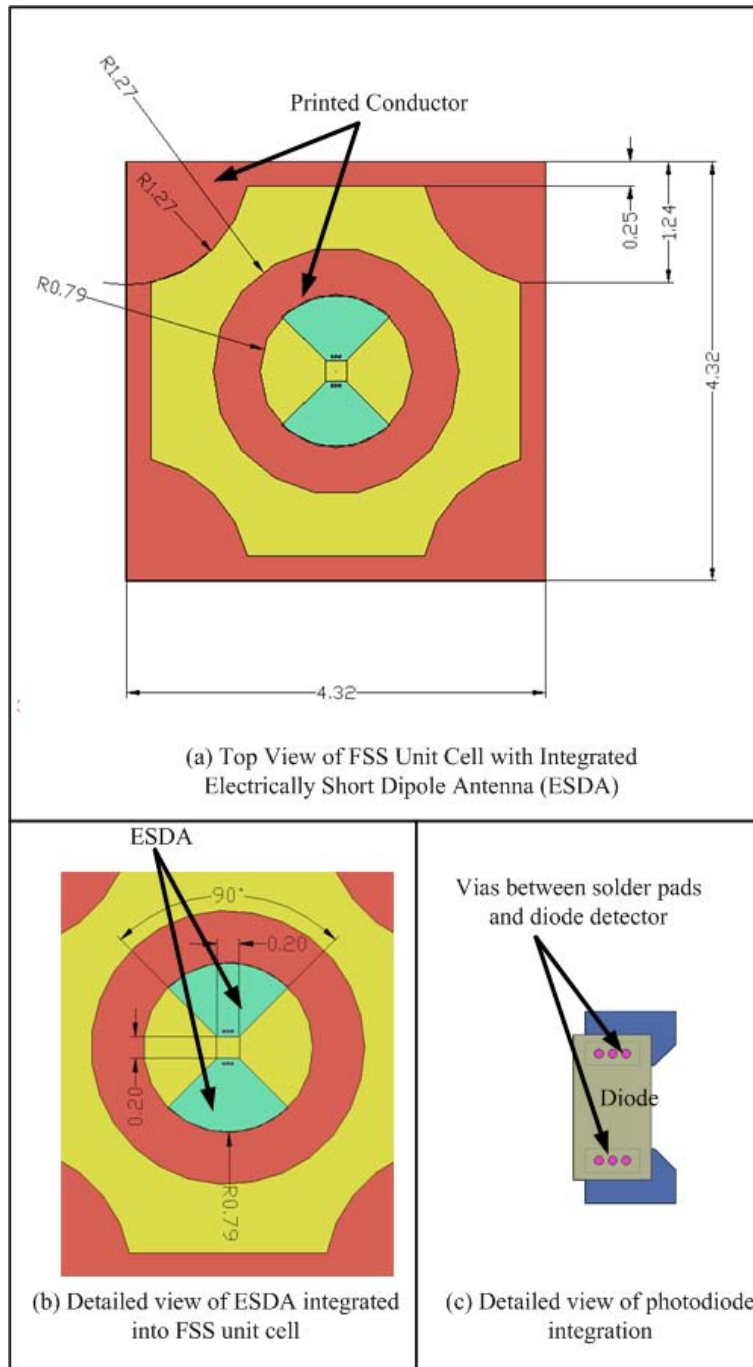


Figure 3-9: Dimensioned drawing of the frequency selective surface (FSS) unit cell with integrated dipole probe and photodiode (units = cm)

A unit cell of the baseline FSS defined in Figure 3-8 was modeled using CST Microwave Studio, a computational electromagnetic (CEM) software package employing the finite integration technique (FIT) [17]. This CEM package contains both a time domain and frequency domain solver. The frequency domain solver was used in these simulations owing to its ability to study off-axis performance for plane wave transmission through a unit-cell of the FSS.

The FSS unit cell simulations focused on two orthogonal TEM modes defined as TE_0 (y-polarized) and TM_0 (x-polarized). The electric field definition for these two modes is provided in Figure 3-10. The transmission coefficient for various scan angles is shown in Figure 3-11. These scans were in the $\varphi=0^\circ$ plane (parallel to the x-axis). This scan represents an E-plane scan for the TE_0 mode and an H-plane scan for the TM_0 mode. The results indicate excellent transmission in the pass band at all scan angles. The performance of the FSS deteriorates slightly at the 45° scan for both the TE and TM mode. In the TE case, the transmission coefficient degrades slightly at the low end of the pass band. Conversely, the TM case experiences a slight performance drop at the high end when scanned to 45° . However, in both cases the performance drop is small indicating that this design will appear transparent to incident waves in the pass band of 2.5-3.5 GHz.

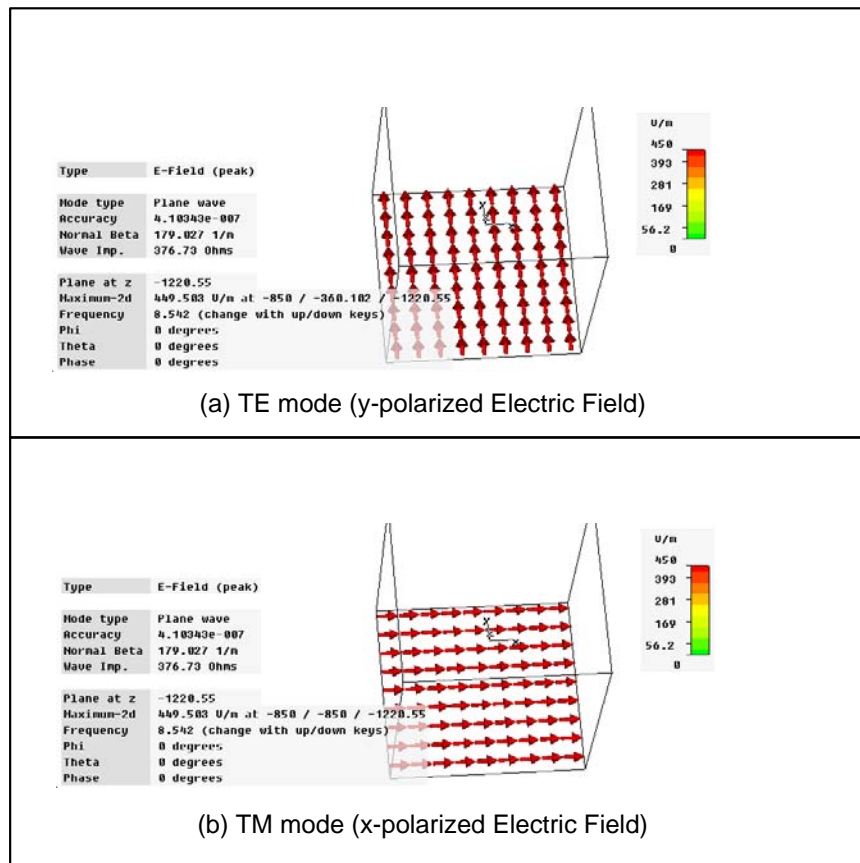


Figure 3-10: Electric field definitions for the TE and TM mode used in simulations of the FSS unit cell

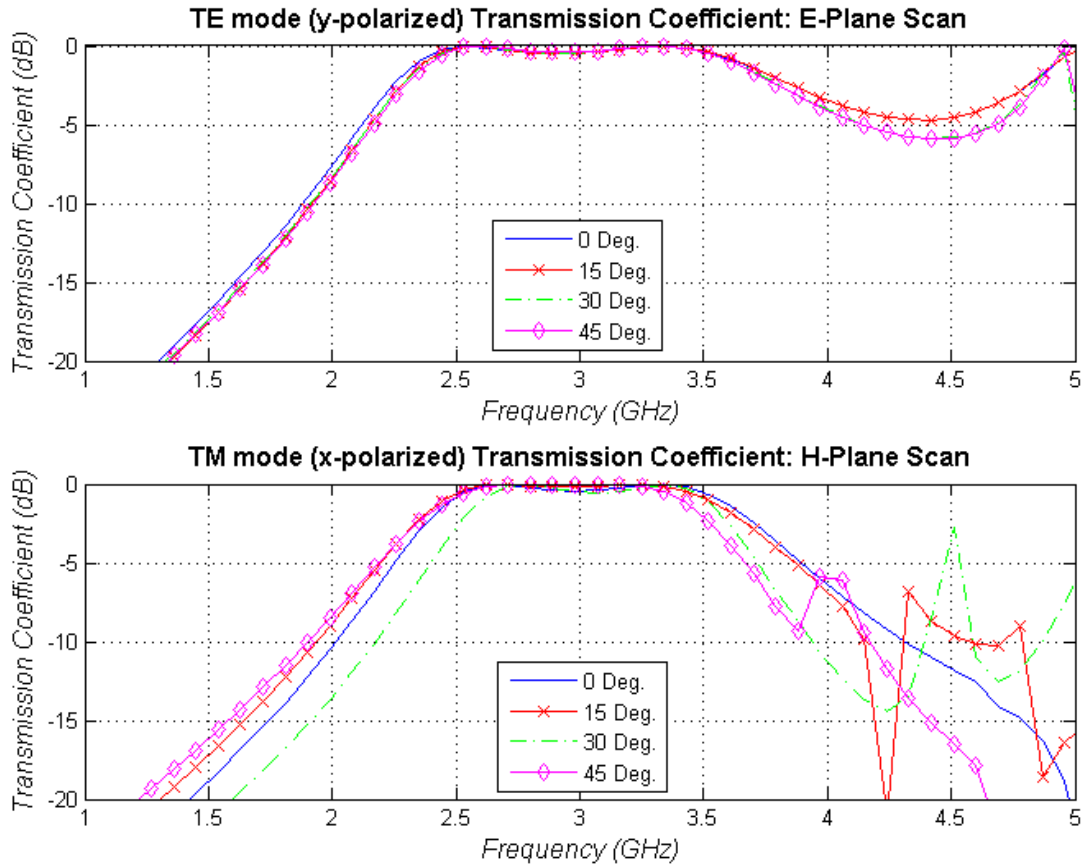


Figure 3-11: Simulated transmission coefficient of FSS unit cell for multiple scan angles

Several FSS panels were constructed to investigate the impact of various ESDA configurations. Three sets of 10x10 panels including various numbers of antennas were constructed. The first panel served as the baseline case, and it contained no antennas. The second panel had ESDA in one row – 10 transmitters total, and the third panel had transmitters on all 100 elements. The PCB layers for the three cases are illustrated in Figure 3-12. The transmission coefficient for the three panel types was measured using a pair of quad-ridged horn antennas and a pair of spot-focusing lenses. The measurement technique is similar to that described in [20]. Time gating was also used to further improve the fidelity of the measurement system by removing the contributions from environmental reflections that occur outside of the primary coupling.

The measured results from Figure 3-13 show two important results. The first observation is that the presence of the electrically short dipole probes did not significantly impact the transmission properties of the FSS panels. The second observation is that the results for all three panels are in good agreement with the simulated results for the unit cell with no probes. The measured FSS show that the transmission efficiency starts to roll off slightly at the high edge of the pass band,

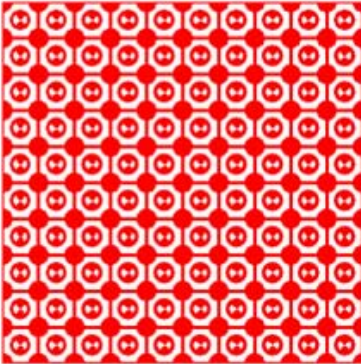
but the measured transmission efficiency is still greater than -2.0 dB across the entire band of interest. These two results indicate that the optical calibration system can be integrated into the FSS panel without significantly degrading transmission performance.



(a) No Probes



(b) 10 Probes



(c) 100 Probes

Figure 3-12: Illustration of the printed circuit board layers for 10 x 10 FSS panels containing (a) 0, (b) 10, and (c) 100 electrically short dipole antenna (ESDA) probes

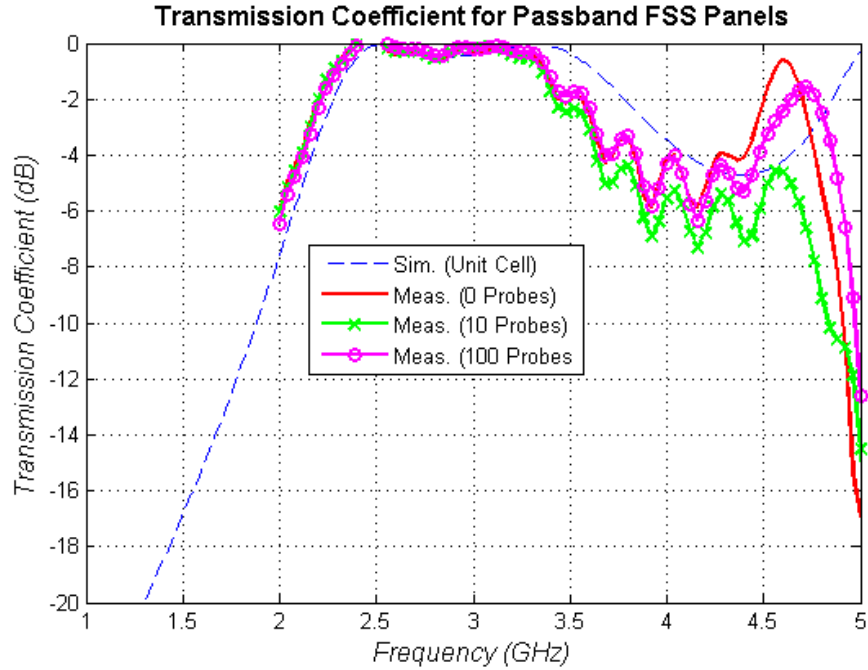


Figure 3-13: Measured transmission coefficient through FSS panels with various numbers of optical calibration probes compared to a baseline unit cell simulation

3.3 Design and Performance of a Broadband Dipole Array

A broadband dipole array was designed to serve as the test array for the optical calibration system. The dipole element is fed using a double Marchand balun. The Marchand balun consists of a microstrip (unbalanced)-to-slotline (balanced) transition. The balun design uses a short-circuited length of slotline and an open-circuited length of microstrip line for maximizing the efficiency of the unbalance-to-balanced transition. The double Marchand balun design presents additional degrees of freedom that can lead to a broader frequency bandwidth. This technique has been shown to yield bandwidths as wide as 100% in dipole designs [21]. An illustration of the dipole element is shown in Figure 3-14.

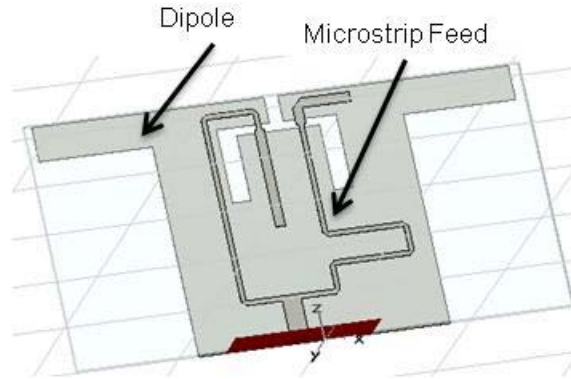


Figure 3-14: Illustration of Broadband Dipole Element fed with Double Marchand Balun

The element was simulated in an infinite array environment using periodic boundary conditions in both the E- and H-plane. The unit cell was selected to be a square with a side length of 4.32cm (1.7”) to match the unit cell of the previously discussed FSS. This allows one ESDA and accompanying photodiode to be present above each element in the array. The simulated results indicate an active element return loss less than 10dB (corresponding to a VSWR < 2.0:1) from 2.5 – 4.0GHz, resulting in a 46% impedance bandwidth. The simulated active element return loss is shown in Figure 3-15.

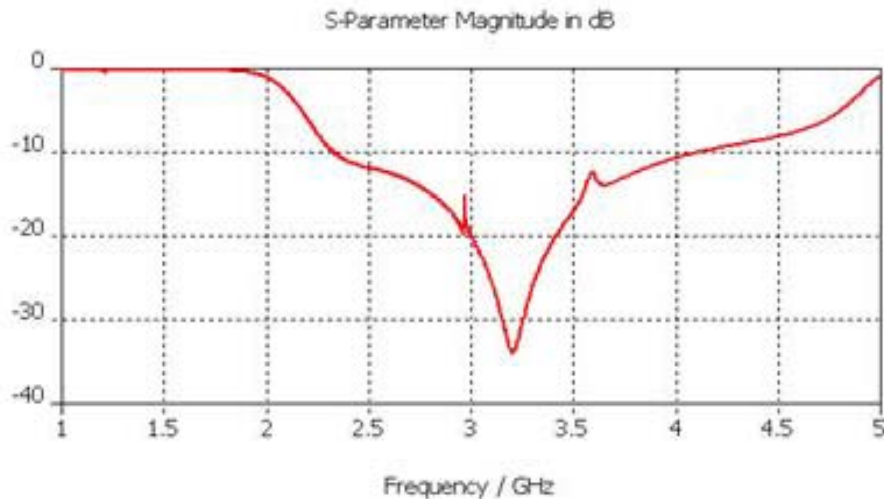


Figure 3-15: Simulated Active Element Return Loss

A 19x18 element array was constructed using the double Marchand balun dipole. Each 18 element row was constructed out of two printed circuit boards, each containing nine elements. A photograph showing the two sides of one of the printed circuit boards is provided in Figure 3-16. The top side of the printed circuit boards contains the ground plane for the feeding microstrip line, the dipole structure, and the two short-circuit slotline sections for the balun. The bottom side of the board contains the microstrip feed.

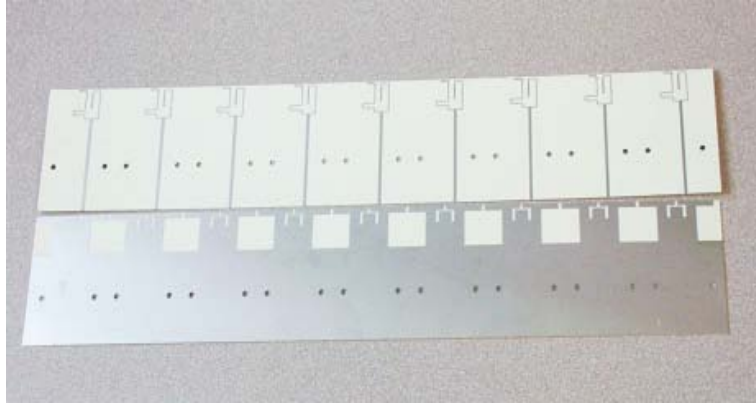


Figure 3-16: Constructed Double Marchand Balun Dipole Elements

The radiation pattern for E-plane line arrays was measured using a near-field scanner. Each line array consisted of 16 dipole elements. The elements were excited with equal amplitude and phase. The remaining two elements in the row were terminated with 50Ω loads to serve as dummy elements. This was done to minimize the impact of edge effects on the outer elements in the row that are generated by asymmetrical mutual coupling. The measured results for three rows of the array are shown in Figure 3-17 for four frequencies within the operational bandwidth of the array: 2.75 GHz, 3.00 GHz, 3.25 GHz, and 3.50 GHz. The results show excellent performance including a broadside pattern with maximum value at $\theta=0^\circ$, the anticipated -13dB sidelobe level (SLL) expected for uniform excitation, and deep nulls.

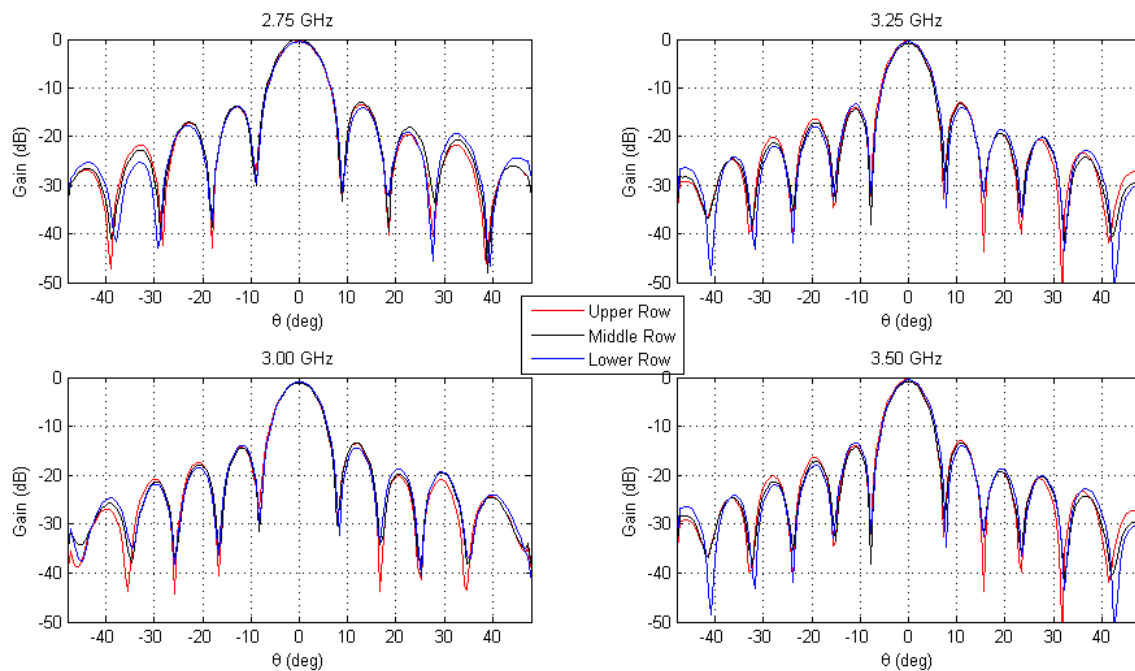


Figure 3-17: Measured radiation patterns for multiple rows of the broadband dipole array fed with a dual Marchand balun

4 SYSTEM PERFORMANCE AND STABILITY

The stability of the optical components and the generated RF calibration signal are essential factors in establishing a confidence level in photonic-based calibration technique. In order for this technique to be viable, the calibration signal must be stable as a function of time and temperature, and the amplitude and phase of the signal must be repeatable. Moreover, the frequency selective surface with integrated photonics must remain RF-transparent within its pass band to avoid degrading the performance of the phased array. This section of the report will detail the experimental verification of the system stability and RF-transparency.

4.1 Photonic System Stability

The amplitude and phase response of the optical calibration probes must be stable over time in order to provide a usable calibration signal. In order to test the stability, the optical FSS panel with integrated probes was placed in a near field range. The near field probe sampled the energy at 16 channels over a seven hour time period to check the stability of the signal with respect to time. This seven hour measurement was repeated five times to investigate the repeatability of the measurement process. All measurements were performed at 3.0 GHz, the center frequency in the operational band of the FSS pass band.

The near field measurements were started prior to powering on the calibration optics to see how long it took the measurements to reach a stable level. The amplitude and phase response for the first measurement are plotted in Figure 4-1. Each plot is divided into two time regions: 1) *Transition Region* and 2) *Stable Region*. The *transition region* is the initial, relatively short, period of time containing the point where the optical calibration signal is powered on. The remaining measurement time is termed the *stable region*. The curves plotted in this figure are calculated using (4-1). The first term in equation (4-1) represents a sliding window average around the current point. The second term defines the average response (amplitude of phase) of the stable region in the measurement. Essentially, this equation is comparing the instantaneous amplitude or phase to the stability response of the system.

$$f_{norm}(t) = \frac{1}{9} \sum_t^{t+9} f(t) - \frac{1}{N_{stable}} \sum_{x_{stable}=1}^{N_{stable}} f(x_{stable}) \quad (4-1)$$

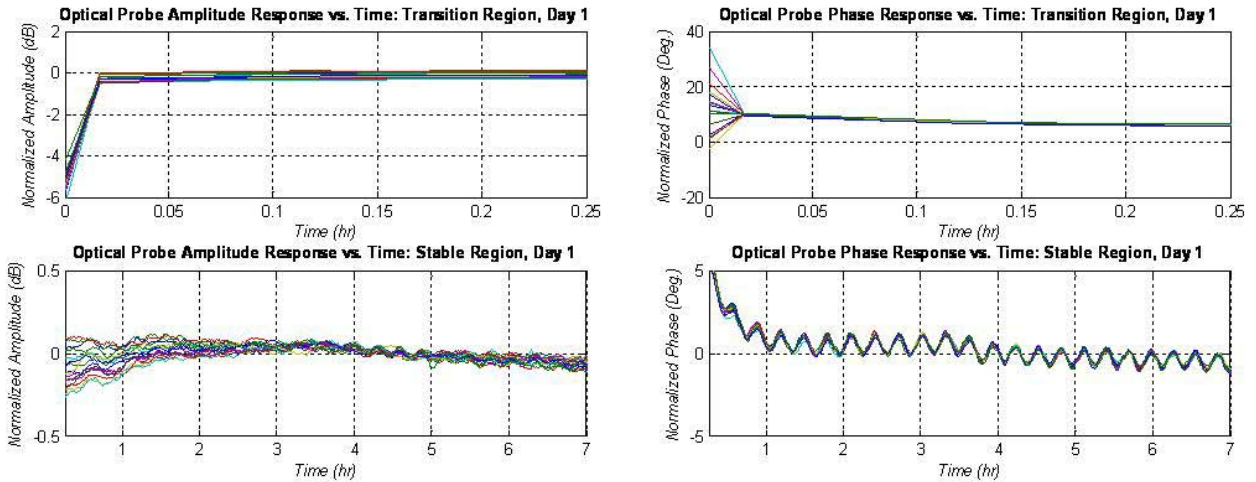


Figure 4-1: Amplitude and Phase Response of Stability Measurement: Day 1

The amplitude and phase response stabilize after a short period of time for the initial measurement set. In order to investigate the repeatability of the system, these measurements were repeated four more times. The normalized response was then calculated for each of the measurements. However, each of the subsequent measurement sets was compared to the stable region average response from the initial measurement set. In doing this, the repeatability and stability of the calibration probes could be established. The normalized results for Day 2-5 are provided in Figures 4-2 through 4-5 respectively.

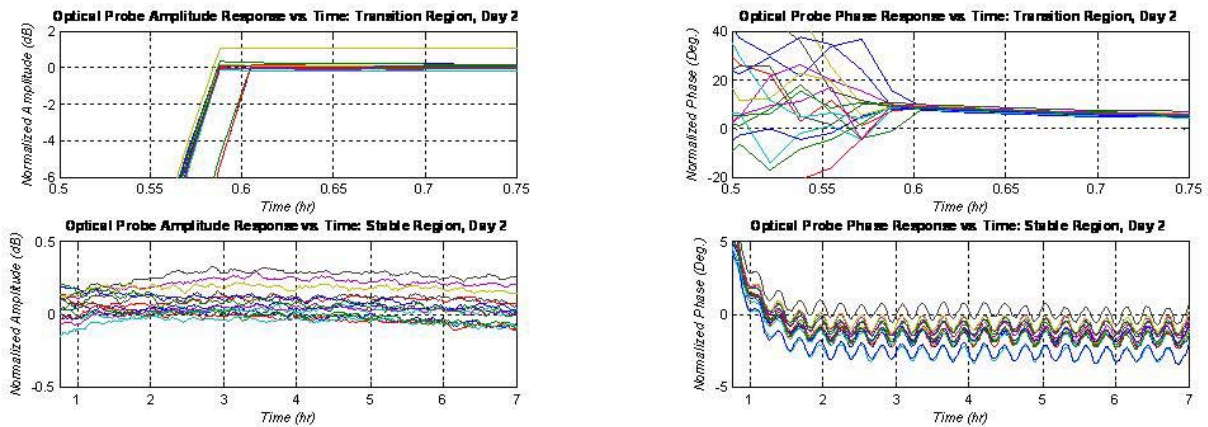


Figure 4-2: Amplitude and Phase Response of Stability Measurement: Day 2

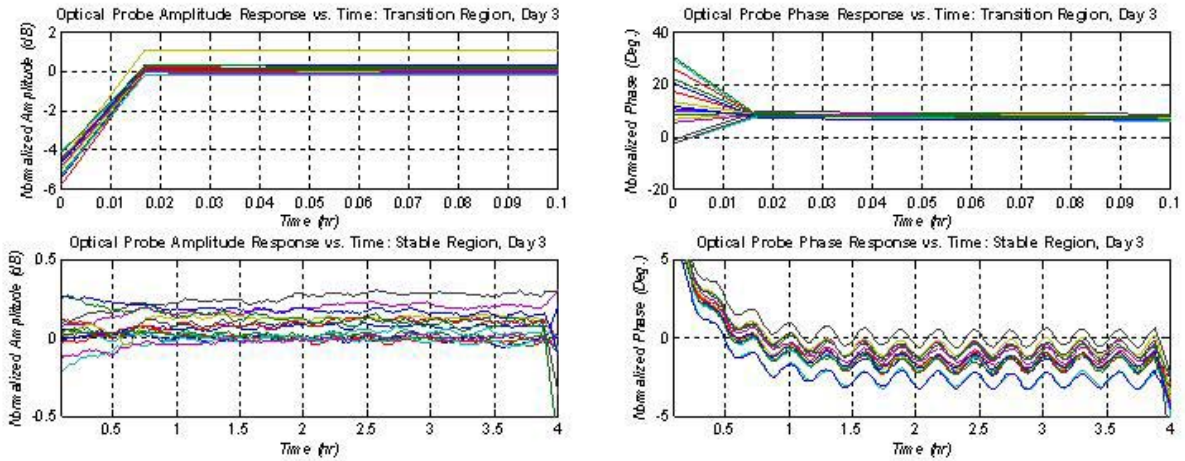


Figure 4-3: Amplitude and Phase Response of Stability Measurement: Day 3

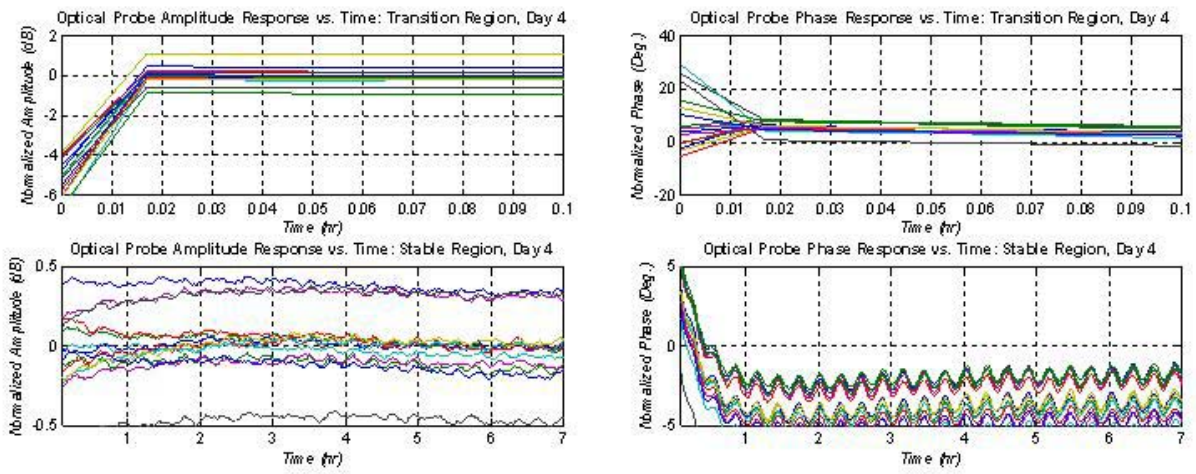


Figure 4-4: Amplitude and Phase Response of Stability Measurement: Day 4

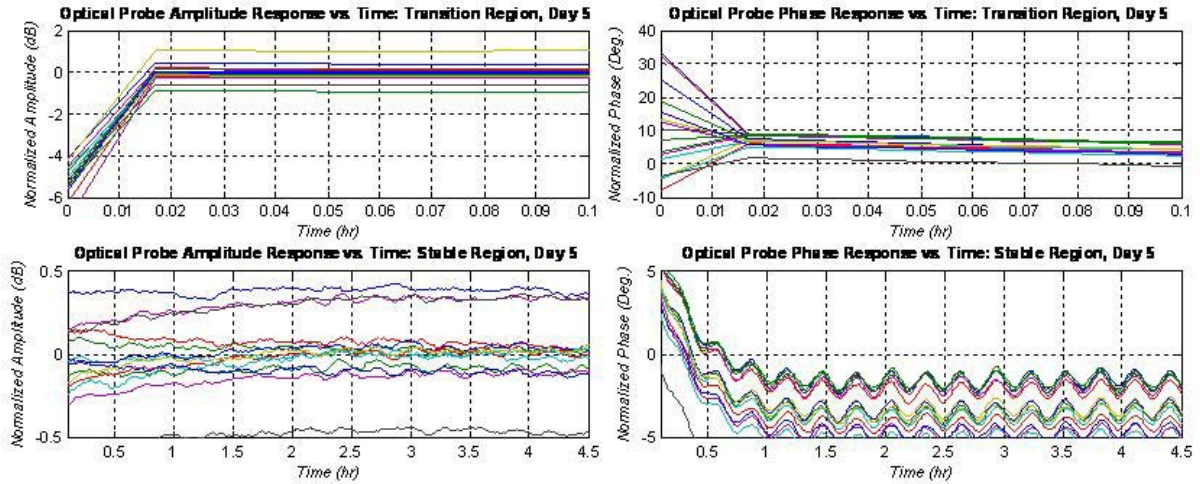


Figure 4-5: Amplitude and Phase Response of Stability Measurement: Day 5

The standard deviation of the amplitude and phase responses was calculated to provide a better understanding of the systems stability. The average value for the initial measurement set was used for each measurement set so that the repeatability of the system would also be revealed from the results. The standard deviation for the initial amplitude and phase response is shown in Figure 4-6. These results show that each of the 16 calibration channels had a standard deviation of less than 0.1dB and 1° over the initial day of measurements.

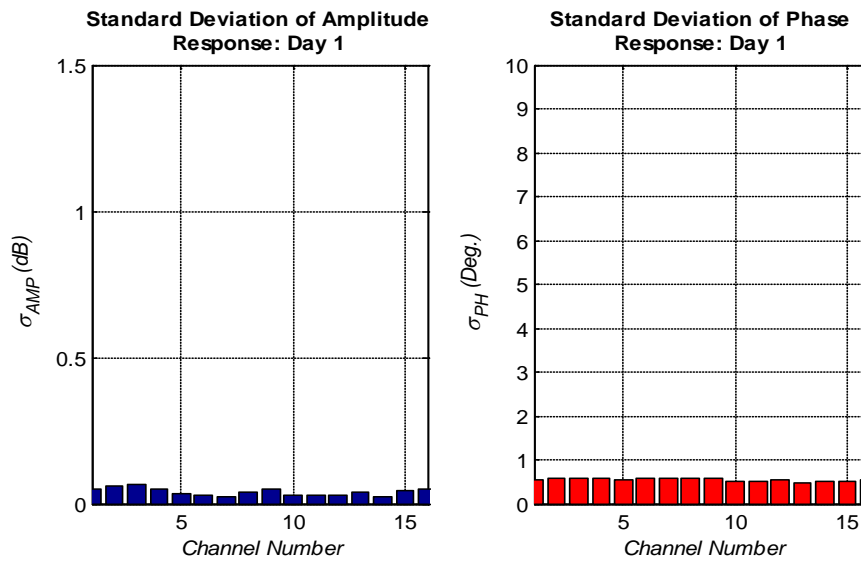


Figure 4-6: Standard Deviation for Initial Amplitude and Phase Response

The subsequent measurement sets were compared to the initial day using equation (4-2). The results are plotted in Figure 4-7 and 4-8. The results show that the calibration system exhibits good stability in both the amplitude and phase of the transmitted signal. With the exception of Channels 6 and 16, the calibration probes have an amplitude standard deviation of less than 0.5dB. The phase response – with the exception of Channel 14 – has a standard deviation of less than 5°. The maximum amplitude standard deviation is 1.3dB, and the maximum phase standard deviation is 8.3°. The curves plotted in Figure 4-8 show that the standard deviation for both the amplitude and phase response are repeatable over the five measurement sets. The optical calibration system can be counted on to have a reliable response time once the system has stabilized. Measurements have shown that the stabilization occurs after a short period of time, on the order of minutes. Once the signal stabilizes, it can remain stable over many hours.

$$\sigma = \sqrt{\frac{1}{N_{stable}} \sum_{x_{stable}=1}^{N_{stable}} \left(f(x_{stable}) - avg(f^{Day1}(x)) \right)^2} \quad (4-2)$$

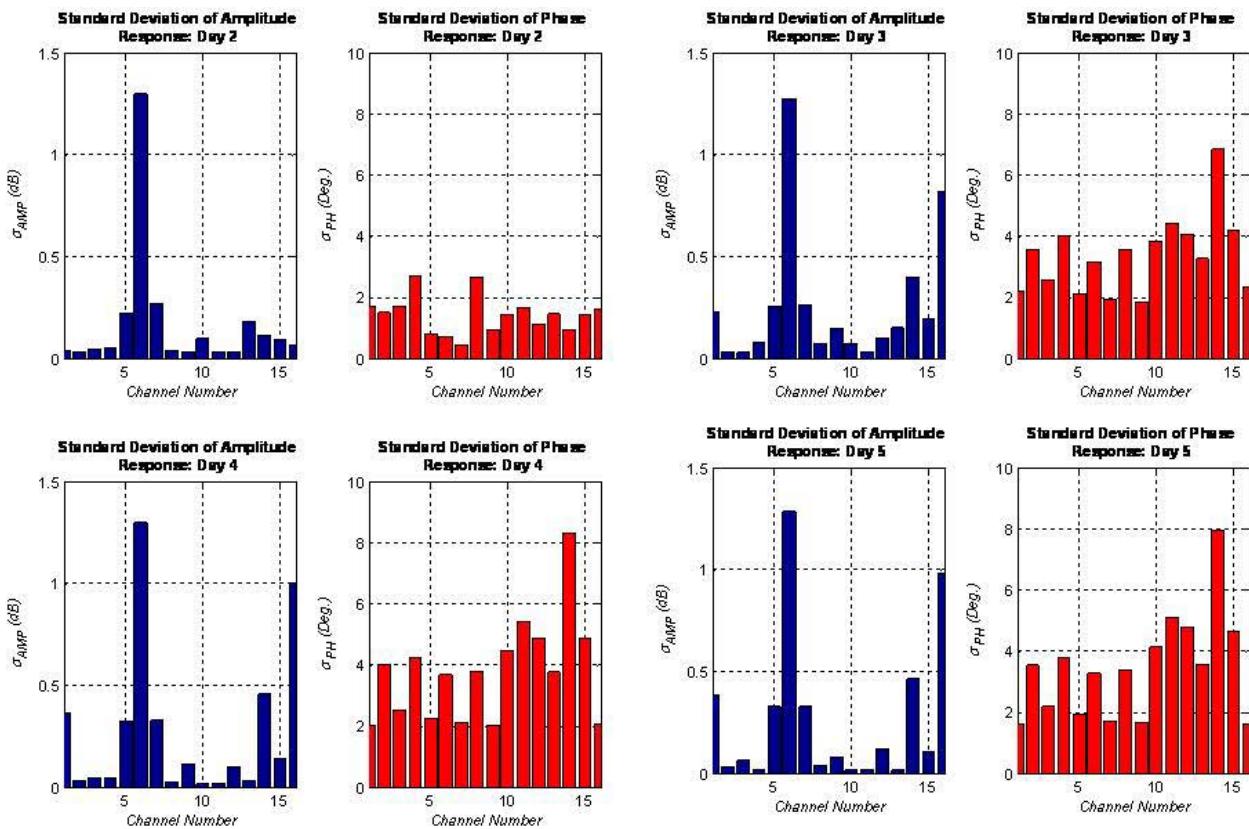


Figure 4-7: Standard Deviation for Amplitude and Phase Response: Day 2-5

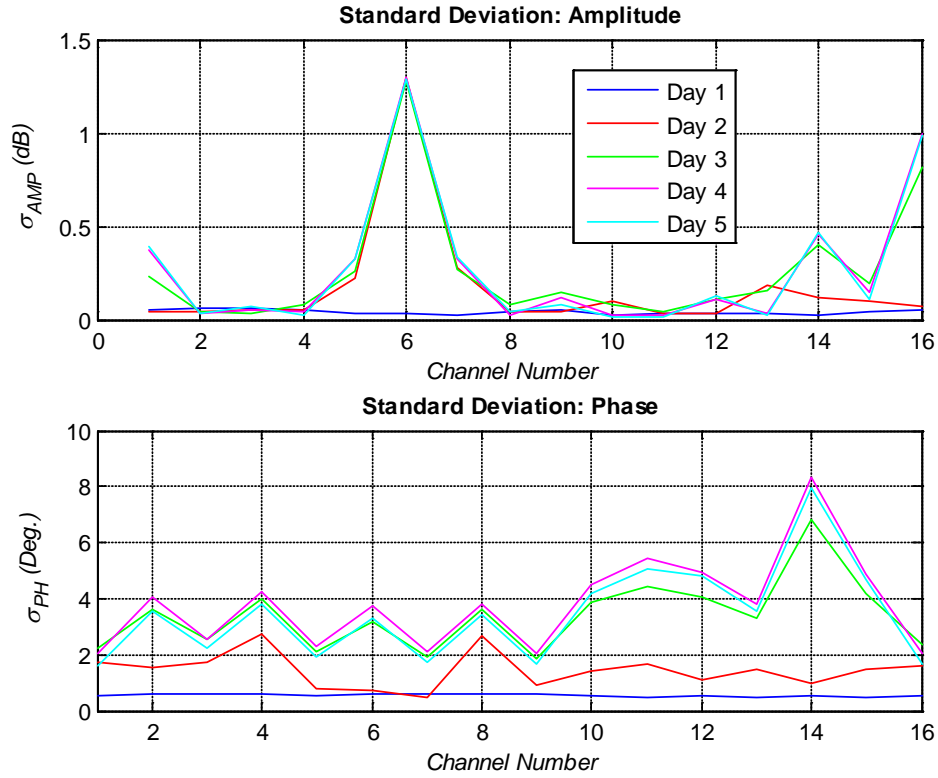


Figure 4-8: Amplitude and Phase Stability

4.2 Stability of Calibration Signal: Photodiode to Antenna Element Coupling

After the optical calibration FSS panel was characterized and seen to be stable, it was then integrated in front of the broadband dipole antenna array as shown in the photograph of Figure 4-9. The calibration system will be based on the coupling from the optical calibration probe to each of the elements in the antenna array. The reliability and repeatability of this coupled signal is essential for the calibration system's fidelity. A measurement set was performed to characterize the coupling to the antenna element. The measurement setup is illustrated in Figure 4-10. Elements 7 and 12 are indicated on this diagram. The results will be provided for these two elements.

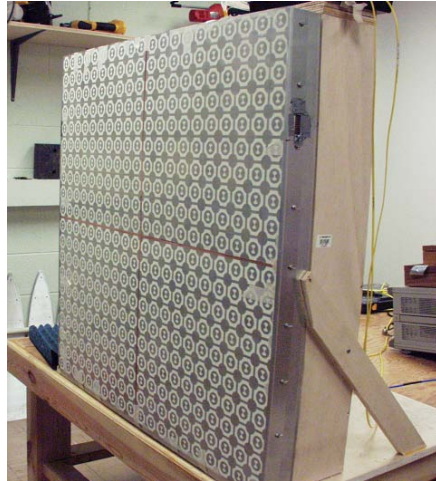
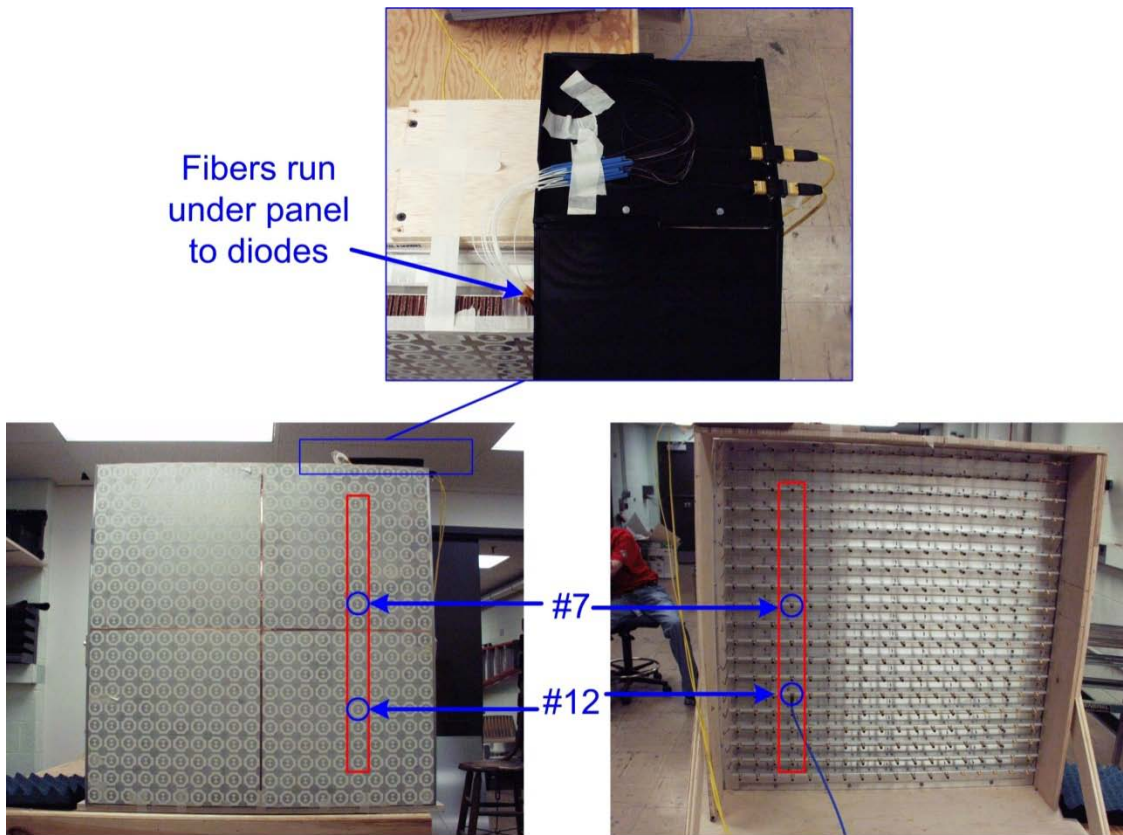


Figure 4-9: Optical Calibration FSS Panel Integrated in Front of Broadband Dipole Array



16 horizontally polarized diodes $\xrightarrow{\text{couple to}}$ 16 horizontally polarized dipoles

Figure 4-10: Optical calibration probe-to-antenna element coupling measurement setup

Optical fibers were run to a vertical column of optical calibration probes. The modulated optical signal was transmitted to the optical probe, at which point it is converted in an RF signal. The RF signal is then transmitted from the optical probe, and it is received by the opposing element in the antenna array. This measurement is treated as a two-port network, and the s_{12} parameter is measured by a network analyzer. The measurements were performed multiple times to make sure that the calibration network is repeatable. The measurement process is illustrated in Figure 4-11.

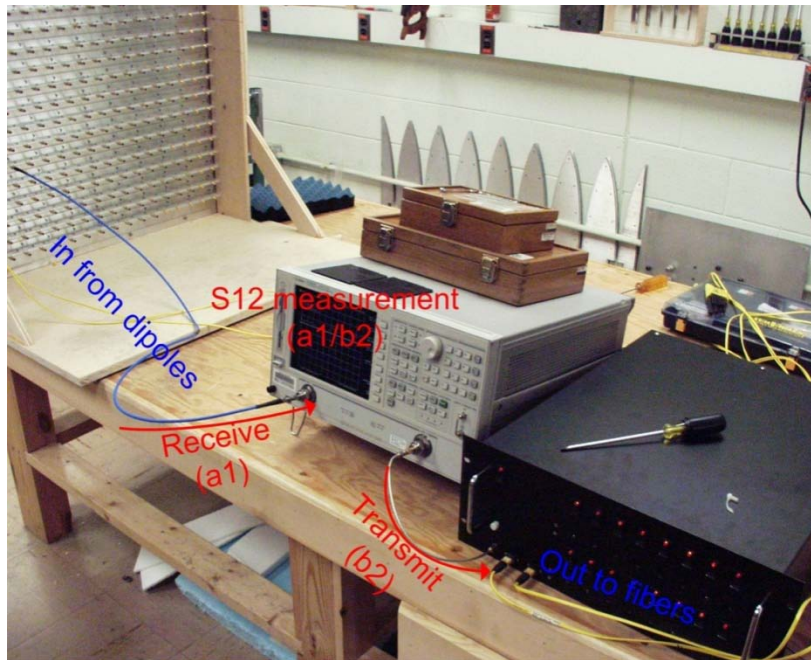


Figure 4-11: Illustration of the s -parameters measured for the optical probe-to-antenna element coupling measurements

The plots of figure 4-12 show the magnitude and phase of the s_{12} measurements averaged over five measurements. The magnitude ranges from -52dB to -58dB. The two elements have similar, but not identical, magnitude and phase responses. However, it is not critical that all channels have identical amplitude and phase responses. Each channel of the photonic calibration network allows static adjustment over both the amplitude and phase. This, the absolute level of the signal can be controlled if needed. The important thing to note is that each channel has a repeatable, and thus predictable, calibration signal. In Figure 4-13, the magnitude and phase of the five s_{12} measurements are normalized to the average result to show the variation.

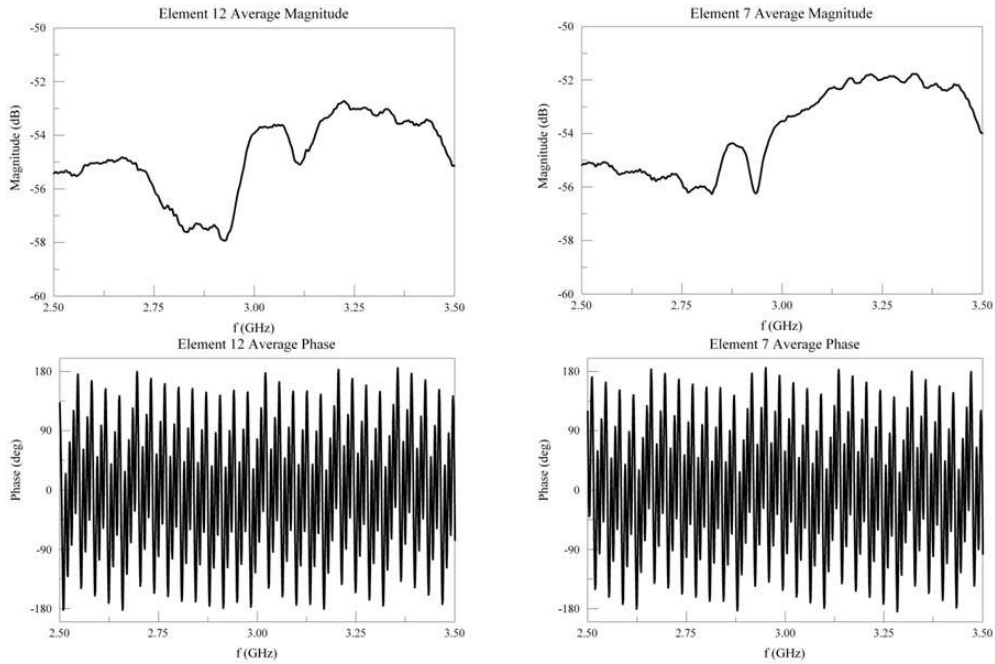


Figure 4-12: Average s_{12} results for optical probe coupling measurements

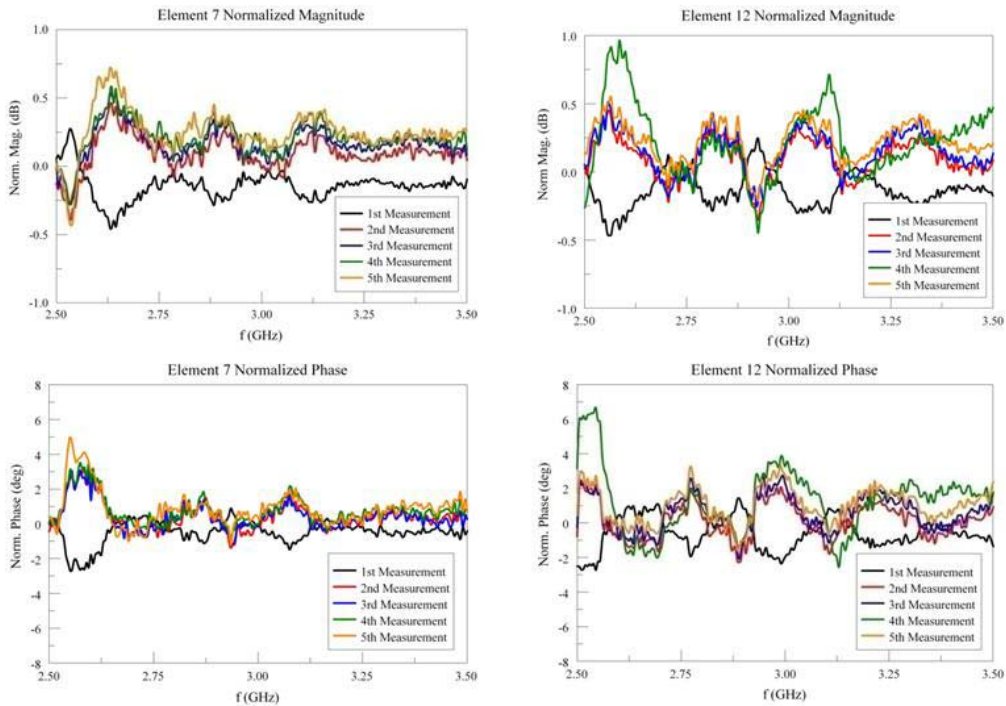


Figure 4-13: Normalized s_{12} results for optical probe coupling measurements

Element 7 showed the most consistent results out of the 16 that were measured. For this element, the magnitude was within 0.5dB of the average, and the phased was within 4° . Element

12 showed the largest variations. The amplitude variation was as high as 1dB, and the phase variation increased to almost 7°. The standard deviation for the mid-band frequency (3 GHz) is plotted in Figure 4-14. All elements have a root mean squared error (RMSE) less than 0.3dB for magnitude and less than 2.5° for phase. Figure 4-15 shows the average RMSE as a function of frequency. The average RMSE increases at the low end of the frequency band, but it is still below 0.3dB and 1.75° across the operational frequency band of the antenna array. This establishes a high confidence level in the repeatability and stability of the optical probe's calibration signal.

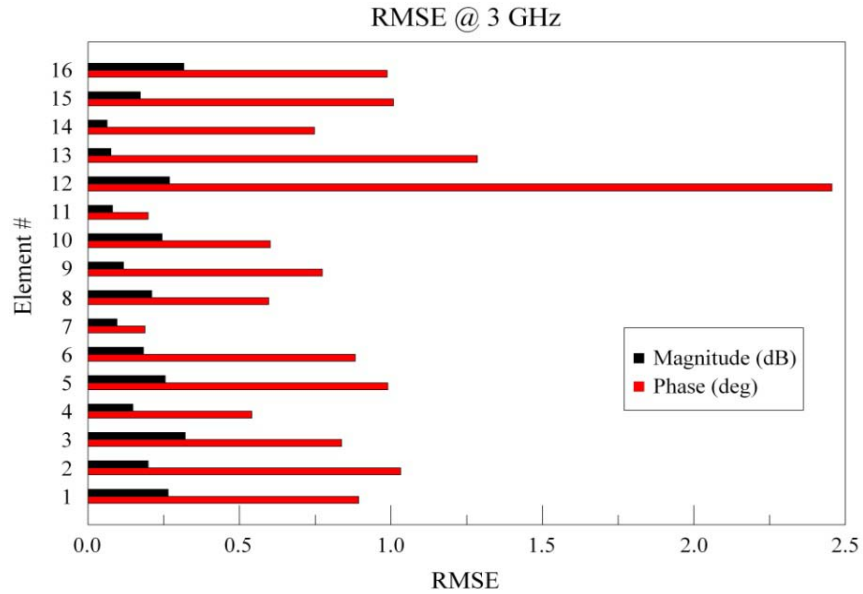


Figure 4-14: Root Mean Squared Error at 3GHz

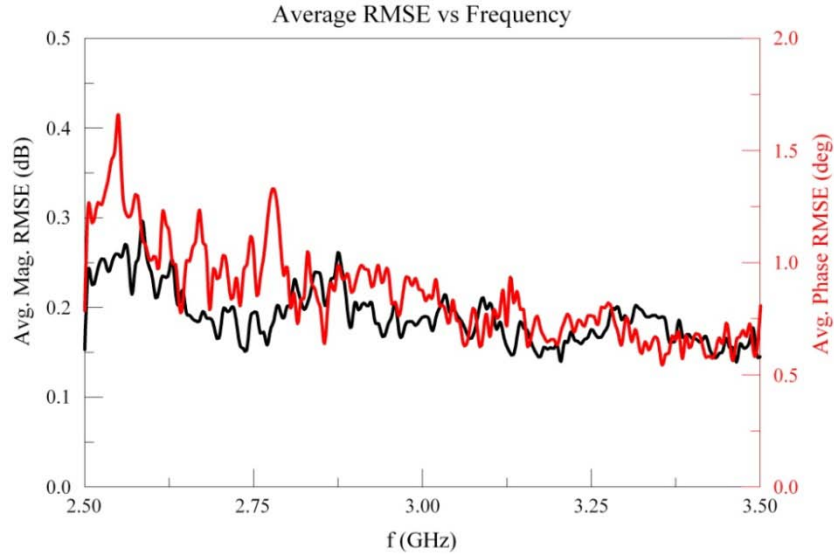


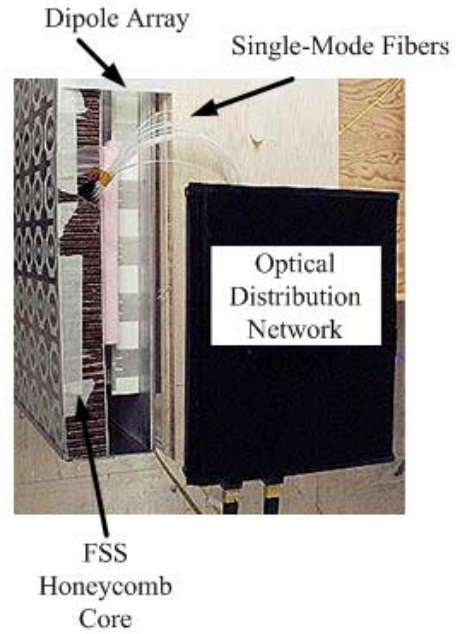
Figure 4-15: Average Root Mean Squared Error vs. Frequency

4.3 RF Transparency of Frequency Selective Surface with Integrated Photonic Calibration System

After the performance of the dipole test array and the FSS were characterized, the FSS radome with integrated ESDA elements was placed $0.25\lambda_0$ in front of a 20x20-element dipole array as shown in Figure 4-16. The radiation pattern of a 16-element row of the array with integrated optical calibration network and FSS was measured in a near-field scanning facility, and the results were compared to the baseline array patterns with no FSS present. This test was completed to see if the components of the optical calibration system would interact with the antenna array elements and impact the transparency of the FSS. The measured results displayed in Figure 4-17 show that the FSS with integrated optical calibration network had minimal impact on the radiation pattern of the dipole array. The patterns are normalized to the baseline case with no optical calibration elements, and no noticeable gain degradation is seen in the measured data. Minimal impact is seen on wide-angle side lobe levels (SLL) at 2.75GHz, and some nulls have filled in slightly. However, the impact on SLL and null depth is minimal. Moreover, the active element impedance match was calculated from measured s-parameters. The results – shown in Figure 4-18 – indicate that the presence of the photonic calibration FSS had minimal impact on the element impedance match.



(a) Front view of the bandpass FSS radome containing the photonic calibration system for phased array antennas



(b) Detailed view showing location of the optical distribution network (ODN) and the single-mode fibers that pass through the honeycomb core of the FSS

Figure 4-16: Photographs of the fabricated frequency selective surface with integrated photonic calibration system for phased array antennas

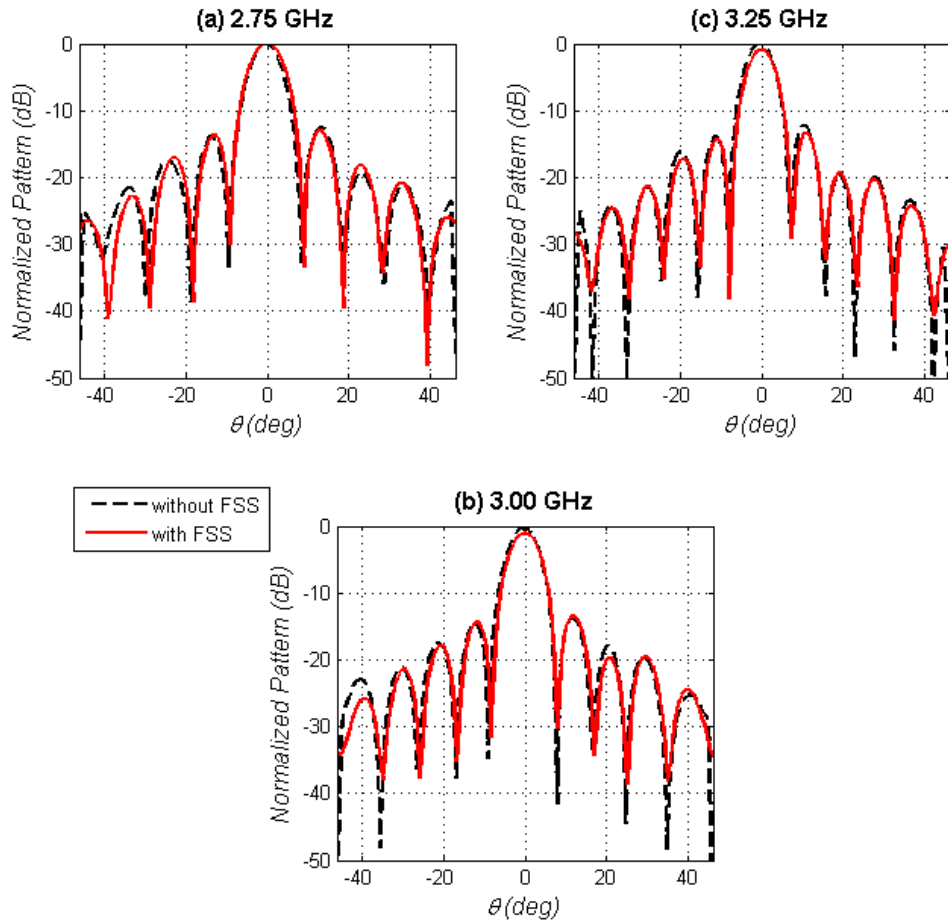


Figure 4-17: Measured radiation pattern of a 16-element dipole array with and without the presence of the FSS with integrated optical calibration system components

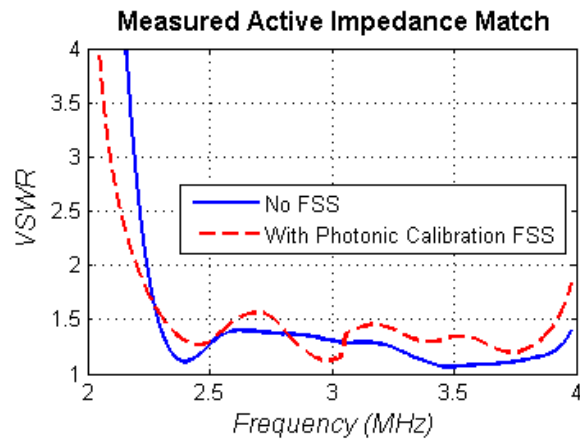


Figure 4-18: Measured active element VSWR for an array element with and without the presence of a frequency selective surface (FSS) with integrated photonic calibration network

5 CONCLUSIONS

This report presents a method for integrating an optical subsystem within a frequency selective surface to provide a calibration system capable of providing in situ compensation for instabilities that can arise within phased array antennas. A zero-biased photodiode is placed across the gap of an integrated electrically short dipole antenna within each unit cell of the FSS. Fibers from an optical distribution network are passed through the honeycomb core of the frequency selective surface and pigtailed to the photodiodes.

A 16-channel calibration system has been successfully demonstrated displaying stability in both RF amplitude and phase. Each channel has a repeatable, and thus predictable, calibration signal. Measurements and simulations show that the FSS with integrated optical network remains RF-transparent. Furthermore, the radiation pattern of a phased array remained unchanged when the array was placed behind the FSS with integrated optics. Subsequently, this FSS enables placement of the calibration system in front of a phased array antenna without impacting the RF performance of the array. These results verify that the photonic calibration network provides a feasible solution for shipboard, in-situ, real-time calibration of phased array antennas. The performance of the 16-channel calibration system has been documented in [22, 23].

The current work demonstrated stable, repeatable calibration performance for a 16-channel photonic system. However, nothing within the system limits the extension to large arrays. As a result, this calibration system exhibits the potential to provide the real-time phase and amplitude equalization necessary for maintaining high fidelity performance in typical large phased arrays used in ship board applications.

REFERENCES

- [1] Hughes, P.; Choe, J.; Zopler, J; "Advanced Multifunction RF System", GOMAC Digest, 194-107 (2000).
- [2] Weijun Yao; Yuanxun Wang; Itoh, T., "A self-calibration antenna array system with moving apertures," Microwave Symposium Digest, 2003 IEEE MTT-S International , vol.3, no., pp. 1541-1544 vol.3, 8-13 June 2003.
- [3] Meyer, R.X.; "Electronic Compensation for Structural Deformations of Large Space Antennas", Astrodynamics Proceedings of the Conference, Vail, CO, August 12-15, 1985. pp. 277-285.
- [4] Lee, E.-A.; Dorny, C.N., "A broadcast reference technique for self-calibrating of large antenna phased arrays," Antennas and Propagation, IEEE Transactions on , vol.37, no.8, pp.1003-1010, Aug 1989.
- [5] Newell, A.C.; "Current state-of-the-art in near-field antenna measurements," presented at Antennas and Propagation Society International Symposium, Boston, Massachusetts, July 8-13, 2001.
- [6] Woollen, D.P.; Snow, J.M.; Tillerson, A.R.; Slowey, W.; Leaf, G.; "Low-Cost Portable Near-Field Antenna Measurement System", Proc. Antenna Application Symposium, pp 310-314, Sept. 16-18, 1998.
- [7] McAdams, G.E.; Romanchuk, R.; "14' x 14' Portable Planar Near-Field Scanner System (PPNFSS) for the Aegis Array", Presented at AMTA99. [Online]. Available: http://www.nearfield.com/amta/AMTA99_1_gma-rr.html.
- [8] Parent, M.G.; Paek, E.G.; Bucholtz, F.; McDermit, C.; Knapp, P.; "Phased-array Calibration using Radome Embedded Optical Transducers," Antenna Application Symposium, Robert Allerton Park, Monticello, IL, pp. 345-360, Sept. 21-23, 2005.
- [9] Godinez, M.E.; McDermit, C.S.; Hastings, A.S.; Parent, M.G.; Bucholtz, F.; "RF Characterization of Zero-Biased Photodiodes", IEEE Journal of Lightwave Technology, vol. 26, no. 24, 15 December 2008, pp. 3829-3834.
- [10] Wake, D.; Walker, N.G., Smith, I. C.; "Zero-bias edge-coupled InGaAs photodiodes in millimetre-wave radio-fibre systems," Electronics Letters, vol. 29, pp. 1879-1881, 1993.
- [11] Pankove, J. I.; Optical Processes in Semiconductors. New York, NY: Dover Publications, 1971.
- [12] Urick, V.J., Rogge, M.S., Bucholtz, F., Williams; "The performance of analog photonic links employing highly compressed erbium-doped fiber amplifiers," IEEE Trans. Microw. Theory Tech., vol. 54, pp. 3141-3145, 2006.
- [13] Esman, R.D.; Williams, K.J.; "Measurement of harmonic distortion in microwave photodetectors," IEEE Photon. Technol. Lett., vol. 2, pp. 502-504, 1990.
- [14] Williams, K.J.; Esman, R.D.; "Observation of photodetector nonlinearities," Electronics Letters, vol. 28, pp. 731-733, 1992.
- [15] Williams, K.J.; Esman, R.D.; Dagenais, M.; "Nonlinearities in p-i-n microwave photodetectors," J. Lightw. Technol., vol. 14, pp. 84-96, 1996.

- [16] Williams, K.J.; Esman, R.D.; Dagenais, M.; "Effects of high space-charge fields on the response of microwave photodetectors," *IEEE Photon. Technol. Lett.*, vol. 6, pp. 639-641, 1994.
- [17] CST Microwave Studio, v.2008.04, 25 Feb 2008.
- [18] Munk, B.A.; *Frequency Selective Surfaces: Theory and Design*, John Wiley & Sons, Inc., New York: 2000, pp. 14-16.
- [19] Wahid, M.; Morris, S.B.; "Band Pass Radomes for Reduced RCS", *IEE Colloquium on Antenna Radar Cross Section*", 7 May 1991, pp. 4/1-4/9.
- [20] Ghodgaonkar, D.K.; Varadan, V.V.; Varadan, V.K.; "A Free-Space Method for Measurement of Dielectric Constants and Loss Tangents at Microwave Frequencies", *IEEE Transactions on Instrumentation and Measurement*", Vol. 37, No. 3, June 1989, pp. 789-793.
- [21] Pickles, W.R.; Dorsey, W.M.; "Proposed Coincident Phase Center Orthogonal Dipoles", *Proc. of 2007 Antenna Applications Symp.*, 18-20 Sept. 2007, Monticello, IL, pp. 106-124.
- [22] McDermitt, C.S., Dorsey, W.M., Godinez, M.E., Bucholtz, F., Parent, M.G., "Performance of a 16-Channel, Photonic, Phased Array Antenna Calibration System", *IEE Electronics Letters*, 19 November 2009, Vol. 45, Issue 24, pp. 1249-1250.
- [23] Dorsey, W.M., McDermitt, C.S.; Bucholtz, F.; Parent, M.G.; "Design and Performance of Frequency Selective Surface with Integrated Photodiodes for Photonic Calibration of Phased Array Antennas", *IEEE Transactions on Antennas and Propagation*, Vol. 58, Issue 8.